Space Science Reviews (2024) 220:85
https://doi.org/10.1007/s11214-024-01119-5

The Polar Stratosphere of Jupiter

V. Hue[1] · T. Cavalié[2,3] · J.A. Sinclair[4] · X. Zhang[5] · B. Benmahi[6] · P. Rodríguez-Ovalle[3] · R.S. Giles[7] · T.S. Stallard[8] · R.E. Johnson[9] · M. Dobrijevic[2] · T. Fouchet[3] · T.K. Greathouse[7] · D.C. Grodent[6] · R. Hueso[10] · O. Mousis[1] · C.A. Nixon[11]

Received: 25 May 2024 / Accepted: 23 October 2024

Abstract
Observations of the Jovian upper atmosphere at high latitudes in the UV, IR and mm/sub-mm all indicate that the chemical distributions and thermal structure are broadly influenced by auroral particle precipitations. Mid-IR and UV observations have shown that several light hydrocarbons (up to 6 carbon atoms) have altered abundances near Jupiter's main auroral ovals. Ion-neutral reactions influence the hydrocarbon chemistry, with light hydrocarbons produced in the upper stratosphere, and heavier hydrocarbons as well as aerosols produced in the lower stratosphere. One consequence of the magnetosphere-ionosphere coupling is the existence of ionospheric jets that propagate into the neutral middle stratosphere, likely acting as a dynamical barrier to the aurora-produced species. As the ionospheric jets and the background atmosphere do not co-rotate at the same rate, this creates a complex system where chemistry and dynamics are intertwined. The ion-neutral reactions produce species with a spatial distribution following the SIII longitude system in the upper stratosphere. As these species sediment down to the lower stratosphere, and because of the progressive dynamical decoupling between the ionospheric flows and the background atmosphere, the spatial distribution of the auroral-related species progressively follows a zonal distribution with increasing pressures that ultimately produces a system of polar and subpolar hazes that extends down to the bottom of the stratosphere. This paper reviews the most recent work addressing different aspects of this environment.

1 Introduction

The four giant planets each possess a hydrogen/helium-dominated atmosphere with a variable amount of heavy elements. Remote-sensing observations allow us to derive a wealth of information on their stratospheres, from the chemical distributions to their thermal structure and dynamics. The stratosphere lies between the deep convective atmosphere, delimited by the temperature minimum around 100 mbar (Robinson and Catling 2014), and the external environment beyond the sub-μbar pressure levels. The chemical distributions are observable clues that reflect the internal chemical processes, but also carry the signature of the interaction with the external environment (through, e.g., external supply, auroral precipitations, etc.), and are influenced by the atmospheric dynamics.

Extended author information available on the last page of the article

Understanding these systems as a whole is complex and requires analyzing each piece of the puzzle individually. Monitoring the chemical distributions is one such piece. Oxygen species broadly derive from external sources (comets, interplanetary dust particles, and interaction with moons/rings) with a smaller contribution from the lower atmosphere. Hydrocarbons however derive from methane photochemistry, and their distribution is controlled by diffusive equilibrium, and seasonal forcing. Observations, when interpreted alongside atmospheric models, provide information on the atmospheric chemical, thermal and dynamical properties.

Stellar and solar occultations in the far-UV allow the thermal profiles and composition of the upper neutral atmosphere to be constrained, including density profiles of molecular hydrogen, methane, ethane and acetylene (Broadfoot et al. 1981; Festou et al. 1981; Greathouse et al. 2010). Radio occultations provide another way to sound the giant planet upper atmospheres. As the signal is progressively refracted by the atmosphere, the change in received radio frequency can be used to infer ionospheric properties (electron density) as well as neutral atmospheric properties such as density, pressure, and temperature (Lindal et al. 1981; Kliore et al. 2004). Mid-infrared (IR) (5-25 μm) emission spectra of the gas giants are characterized by a high density of rovibrational lines from various light gases (CH_4, NH_3, PH_3, C_2H_2, C_2H_4, C_2H_6), and higher-order hydrocarbons such as C_3H_8, CH_3C_2H, C_4H_2, C_6H_6 (e.g. Fletcher et al. 2009; Guerlet et al. 2009, 2010; Sinclair et al. 2019; Roman 2023). At longer wavelengths, in the millimeter (mm)/sub-millimeter range, individual rotational lines can be resolved due to the lower spectral line density combined with the very high resolving power offered by heterodyne spectroscopy. The resolved lineshapes in the mm/sub-mm range and at high-spectral resolution in the mid-IR provide constraints regarding the vertical distribution of the observed species.

Many of the aforementioned observations have been carried out via constantly evolving ground- and space-based observing capabilities. In the mid-IR, a large range of instruments and telescopes have been used to obtain spectroscopic and medium- to narrow-band filtered radiometric observations of Jupiter over the last four decades. Ground-based observatories have allowed the measurement of hydrocarbon emissions in the mid-IR at spectral resolutions R on the order of 10^3 ($R = \lambda/\Delta\lambda$), (e.g. Gillett et al. 1969; Ridgway 1974; Encrenaz et al. 1978; Sada et al. 1998; Moses et al. 2005a). Higher spectral resolutions ($R > 10^4$) have been achieved using IR heterodyne spectroscopy techniques (Kostiuk et al. 1989; Livengood et al. 1993), or with Fourier Transform Spectrometer (Ridgway and Brault 1984) and grating spectrographs (Lacy et al. 2002). Space-based instruments, such as the Infrared Interferometer Spectrometer and Radiometer (IRIS) on Voyager (Hanel et al. 1979b,a), the Short-Wavelength Spectrometer (SWS) on the Infrared Space Observatory (ISO) (de Graauw et al. 1996), or the Composite Infrared Spectrometer (CIRS) on Cassini-Huygens (Kunde et al. 1996, 2004) provided mid-IR spectroscopic observations of Jupiter at high sensitivity (ISO) or with unprecedented spatial resolution at their times (Voyager and Cassini), despite being at more modest spectral resolutions (R $<$ 3000) than recent ground-based observations. First results from the James Webb Space Telescope are currently being published and will be discussed further in this paper (Hueso et al. 2023; Rodríguez-Ovalle et al. 2024).

Similarly, millimeter observatories have evolved drastically, starting with spatially unresolved millimetric observations with the Odin telescope (Cavalié et al. 2008, 2012; Benmahi et al. 2020), and observations containing only a few resolution elements across the Jovian disk with the James Clerk Maxwell telescope (JCMT) and IRAM-30m telescope (Lellouch et al. 1995, 1997; Moreno et al. 2003). Large interferometric facilities such as the Atacama Large Millimeter Array (ALMA) and the Northern Extended Millimeter Array (NOEMA) now combine high spectral and spatial resolution observations of the gas giants (Cavalié

et al. 2021; Benmahi et al. 2022) resulting in an improved understanding of the different processes occurring at low- and polar latitudes affected by the auroral activity.

Spacecraft missions, such as Pioneer, Voyager, Galileo, Cassini-Huygens and Juno, have provided valuable observations of Jupiter's upper atmosphere across a range of spectral windows, in particular on the night sides of the outer planets, inaccessible to ground and Earth orbiting telescopes (e.g. Bolton et al. 2017). Unlike ground-based observations, spacecraft are able to observe the planet's nightside as well as the dayside and have the opportunity to obtain high spatial resolution measurements. The Juno mission has provided a particularly unique view of Jupiter due to its highly eccentric polar orbit; Jupiter's low obliquity (3.13°) means that only limited views of Jupiter's poles can be obtained from Earth's vantage point, so the observations obtained by Juno have transformed our understanding of Jupiter's polar atmosphere (Bolton et al. 2017).

This paper summarizes the current knowledge of Jupiter's upper atmospheric chemical distributions and dynamics, with a focus on polar latitudes, as derived from ground- and space-based observations acquired over the last decades. Jupiter's polar regions host one of the most extreme planetary environments in the solar system. The magnetosphere-ionosphere interaction resulting from its powerful magnetic field, coupled with plasma-rich nearby magnetospheric environment broadly affect the high-latitude thermal structure and chemical distributions, as reviewed here. Auroral particle precipitation produces some of the brightest auroras, as observed across wavelengths ranging from X-ray to radio. Elevated stratospheric temperatures due to charged particle precipitation have been measured for decades using ground- and spaced-based observations, as well as the consequences of this coupling for the high-latitude chemical and dynamics.

First, we review the measured chemical distributions while emphasizing the spatially resolved observations that include the high-latitude regions. Next we discuss the various existing models (photochemical models, ion-neutral chemical models, and aerosol formation models) that aim to explain these distributions. Third, we discuss observations constraining the magnetosphere-ionosphere coupling through measurements of upper atmospheric winds. Finally, remaining outstanding questions will be summarized and discussed.

2 Stratospheric Chemical Distributions

2.1 Hydrocarbons

2.1.1 Constraints from Mid-IR Observations

One of the prime wavelength ranges to monitor hydrocarbon emissions is the mid-IR, as, e.g., observed earlier from the Voyager 1 and 2 missions, or using space telescopes such as ISO (Encrenaz et al. 1996; Fouchet et al. 2000). The mid-IR is an important wavelength region containing spectral signatures of many atmospheric species that contribute to regulate the stratospheric radiative balance (e.g. Roman 2023). The main drawback is the degeneracy between temperature and abundances of the observed species, as they produce similar effects on spectra, and both are physically plausible in auroral regions. Studies discussed in this section make different assumptions about temperature profiles.

Measurements made with IRIS on Voyager 1 and 2 provided some of the first spatial information about the hydrocarbon distribution (Hanel et al. 1979b,a). These observations indicated a general mid-IR polar brightening, reflecting either an enhancement in stratospheric temperature and/or an increase in the hydrocarbon abundances (Kim et al. 1985;

Drossart et al. 1993). The presence of these stratospheric regions with elevated thermal emissions (nicknamed *hot spots*) was similarly detected using ground-based facilities (Caldwell et al. 1980; Orton et al. 1991), or prior Voyager data. By deriving a thermal profile in the polar region required to fit the CH_4 emissions, whose abundance was assumed to be constant across the planet, Kim et al. (1985) measured an abundance enhancement with respect to mid-latitudes. In the polar IR-bright region (averaging latitudes $> 48°$N and longitudes 120-240°W), they derived abundance enhancement factors of $\sim$3 and $\sim$2 with respect to the mid-latitudes (averaging latitudes 30°S-0°, excluding longitudes 120-220°W), for C_2H_2 and C_2H_6, respectively. They also derived abundance measurements of C_2H_4, C_6H_6, and CH_3C_2H in the northern polar region, though only upper limits for these molecular abundances were previously derived at mid-latitudes.

Ground-based observations using infrared heterodyne spectroscopy techniques allowed further investigation of the C_2H_x emissions in the polar regions of Jupiter. Livengood et al. (1993) and Kostiuk et al. (1993) were able to derive scaling factors of the C_2H_6 and C_2H_4 abundances needed to reproduce the observed spectra, assuming a temperature profile based on Voyager 2 IRIS data recorded several years prior. However, because of the degeneracy between temperature and hydrocarbon abundances (also illustrated by Drossart et al. 1993), these studies provided a range of acceptable temperature and hydrocarbon abundances within the auroral regions. Another challenging aspect of measuring spatial trends in polar hydrocarbon emissions using ground-based telescopes relates to the observation geometry. Because of Jupiter's small obliquity (3.13°) combined with the rather small magnetic dipole tilt (10.2°, according to the Juno prime mission model of Connerney et al. 2022), the auroral regions are only observable at high-emission angles during a fraction of the Jovian rotation. Additionally, Jupiter's magnetic field is asymmetric, and the northern aurora extends more equatorward than the southern one, making the former one easier to observe from Earth.

IR measurements were similarly acquired using the Cassini/CIRS instrument during the December 2000 Jupiter flyby (Kunde et al. 2004). Nixon et al. (2007) retrieved the meridional variations of temperature, as well as the C_2H_2 and C_2H_6 abundances in the 70°S-70°N range. Temperatures were derived from spectral features of H_2 and CH_4. The continua at 600–670 cm^{-1} (14.9-16.6 μm) and 760–800 cm^{-1} (12.5-13.2 μm) are due to the broad H_2 S(1) line, and were used to retrieve the upper-tropospheric temperature, while assuming a constant H_2 gas abundance. The CH_4 ν_4 band at 1225–1325 cm^{-1} (7.5-8.2 μm) was used to retrieve the stratospheric temperatures. The C_2H_2 and C_2H_6 abundances were subsequently retrieved using their respective ν_5 band at 670-760 cm^{-1} (13.2-14.9 μm) and ν_9 band at 800-850 cm^{-1} (11.8-12.5 μm). The main contributions to the C_2H_2 and C_2H_6 emissions are located around 5 mbar, with C_2H_2 contributions extending up to 0.1 mbar and 10 μbar.

At high-latitude, Nixon et al. (2007) derived the meridional distribution of C_2H_2 and C_2H_6 while zonally averaging the CIRS-acquired spectra. CIRS revealed an enhancement in the emission of several hydrocarbons around a large region located near the magnetic poles of Jupiter. Consequently, Nixon et al. (2007) excluded from their zonal average spectra recorded at 60°S-70°S and 330-90°W, as well as 60°N-70°N and 150-210°W, where such hot spots had been repeatedly identified. Note that throughout this document, all quoted latitudes are planetocentric. At 5 mbar in the stratosphere, Nixon et al. (2007) found that the C_2H_2 and C_2H_6 meridional trends are mainly anticorrelated, with C_2H_2 decreasing with increasing latitude, while C_2H_6 peaks at $\pm 70°$. This result poses a dilemma as both hydrocarbons are by-products of the methane photolysis and therefore should follow similar spatial trends (see Sect. 3.1 for a model/data comparison). The anti-correlated trends were then assumed to be caused by a difference in chemical lifetime between these two molecules.

Nixon et al. (2010) subsequently performed a detailed C_2H_2 and C_2H_6 spectral modeling of the IRIS measurements obtained during the Voyager 1 flyby of Jupiter in 1979. Using a similar retrieval method, they confirmed the finding from Nixon et al. (2007) while reanalyzing both datasets using an updated spectral database for ethane. Extending the analysis of the CIRS dataset, Sinclair et al. (2017) retrieved the temperature, C_2H_2, C_2H_4 and C_2H_6 distributions as a function of latitude and longitude, including in the auroral hot spot region. They tested the robustness of the temperature retrieval using several thermal a priori profiles with variable upper stratospheric temperatures. They found, using both Cassini/CIRS high ($\Delta\nu = 0.5$ cm^{-1}) and medium ($\Delta\nu = 2.5$ cm^{-1}) spectral setup the presence of localized hot spots at two different pressure levels ($\sim$10 μbar and $\sim$1 mbar) with elevated stratospheric temperatures on the order of 20 K and 10 K, respectively, though the exact magnitude was found to depend on the spectral setup of the instrument. The Voyager/IRIS measurements, on the other hand, did not support the existence of that double-peaked localized heating regions, which was attributed to a lack of sensitivity due to IRIS' lower spectral resolution.

Sinclair et al. (2017) further studied the enhancement in C_2H_6 and depletion in C_2H_2 at non-auroral high-latitudes. Above Jupiter's main UV-auroral ovals, they additionally showed a localized $\sim$15% enhancement of C_2H_2 in the 1-5 mbar range while also showing a depletion in C_2H_6, despite rather large error bars. Sinclair et al. (2017) showed a key figure (their Fig. 13) demonstrating that, at 70°N, the combined amount of $C_2H_2 + C_2H_6$ stayed constant as a function of longitude, while the local enhancement and depletion of these two hydrocarbons compensating for each other in the longitudinal region of the main oval. They suggested that C_2H_2 may be locally produced within the auroral region and converted into C_2H_6 outside of the oval.

Sinclair et al. (2019) extended the modeling of the Voyager/IRIS and Cassini/CIRS datasets by analyzing the emissions from further hydrocarbons: ethylene (C_2H_4) around 950 cm^{-1} (10.5 μm), methylacetylene (CH_3C_2H) around 632 cm^{-1} (15.8 μm), diacetylene (C_4H_2) around 628 cm^{-1} (15.9 μm), and benzene (C_6H_6) around 674 cm^{-1} (14.8 μm). In the auroral regions, they found that abundance enhancements of 6.4 and 9.6 in C_2H_4 and C_6H_6 with respect to photochemical model A of Moses et al. (2005a) were needed to reproduce the high-spectral resolution ($\Delta\nu = 0.5$ cm^{-1}) CIRS spectra. Similarly, auroral enhancements of 1.6, 3.4 and 15 in the abundances of C_2H_4, CH_3C_2H, and C_6H_6, respectively, were needed to reproduce the medium resolution CIRS spectra ($\Delta\nu = 2.5$ cm^{-1}). Only an upper limit of C_4H_2 was found in the auroral and non-auroral regions.

Some of these findings triggered subsequent ground-based observing campaigns at higher spectral resolving power using the Texas Echelon Cross Echelle Spectrograph (TEXES) instrument (Lacy et al. 2002), mounted on the NASA Infrared Telescope Facility (IRTF) or the Gemini-North telescope (Sinclair et al. 2020, 2023). TEXES allowed the derivation of the meridional distribution of acetylene and ethane across Jupiter, confirming the general equator-to-pole decrease/increase in the C_2H_2/C_2H_6 abundances, respectively found by Cassini-CIRS (Fletcher et al. 2016; Melin et al. 2018). In the polar regions, despite the slightly less favorable viewing geometry than with Voyager or Cassini, TEXES observations permitted the derivation of the high-latitude temperature, C_2H_2, C_2H_4, and C_2H_6 abundance profiles. Figures 1 and 2 provide a snapshot at the Gemini-N/TEXES observations published by Sinclair et al. (2023). They confirmed (i) the presence of the localized heating in the auroral region at two discrete pressure regions of 1 mbar and 10 μbar, (ii) the localized enhancement of C_2H_2, C_2H_4 within the auroral region, and (iii) enhancement in the C_2H_6 abundance over a large longitudinal range at high-latitude in the north polar region. Sinclair et al. (2023) also suggested that the local enhancements in temperature and hydrocarbons may be even more localized within the auroral region following a solar wind compression event.

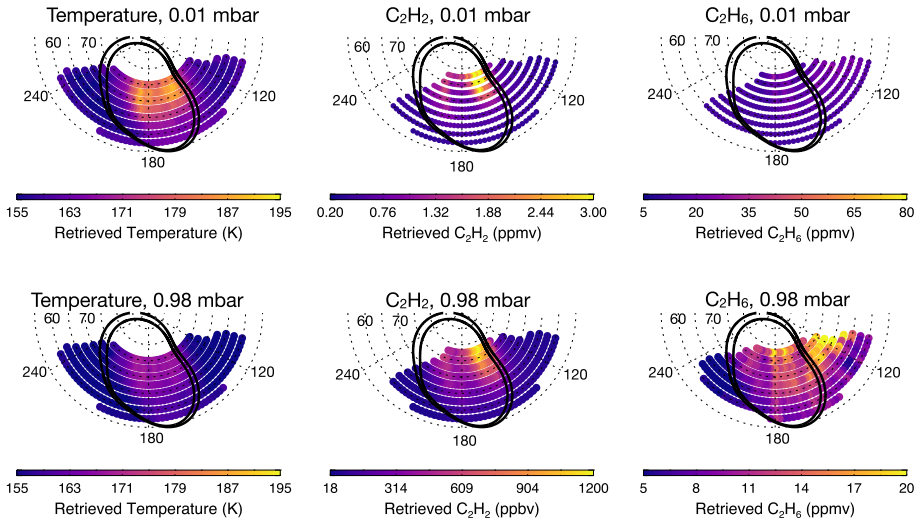

Fig. 1 Northern polar projection of the retrieved temperature (left), C_2H_2 (center) and C_2H_6 (right) abundances at 0.01 mbar and 0.98 mbar on 2017 March 19 from Gemini-N/TEXES (Sinclair et al. 2023). The contracted and expanded reference UV auroral oval derived from HST observations are displayed in solid black line (Bonfond et al. 2012)

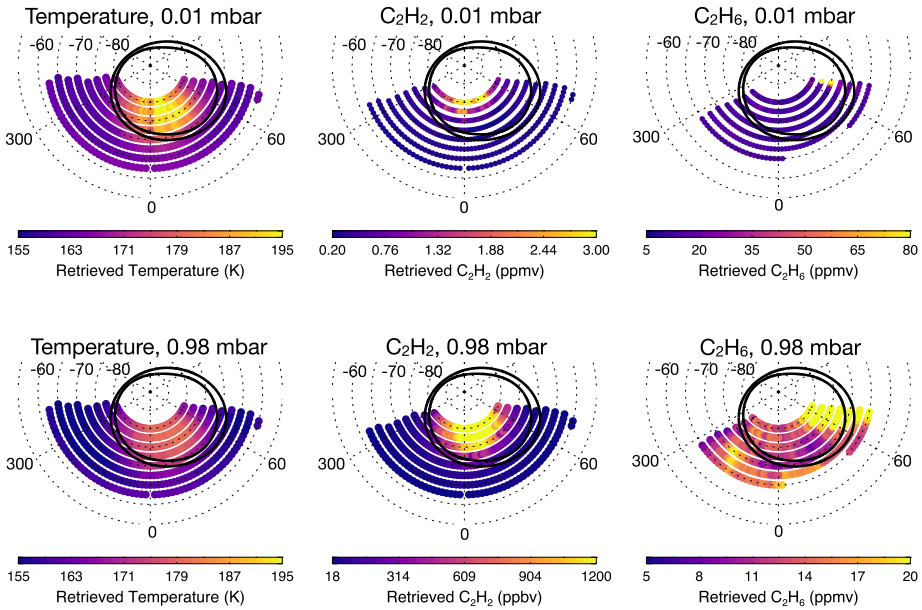

Fig. 2 Same as Fig. 1 for the southern hemisphere, from Sinclair et al. (2023)

The James Webb Space Telescope has recently been providing new mid-IR observations of Jupiter, using the medium resolution spectroscopy modes (MIRI-MRS), as part of the Early Release Science ERS 1373 program. Rodríguez-Ovalle et al. (2024) retrieved the

Table 1 Summary of Jovian acetylene (C_2H_2) measurements. [1] Nixon et al. (2010) ; [2] Sinclair et al. (2017) ; [3] Nixon et al. (2007) ; [4] Fletcher et al. (2016) ; [5] Melin et al. (2018) ; [6] Sinclair et al. (2018) ; [7] Giles et al. (2021a) ; [8] Giles et al. (2023) ; [9] Sinclair et al. (2023) ; [10] Rodríguez-Ovalle et al. (2024)

Instrument	Coverage	Trend	Ref
Voyager/IRIS	57°S-56°N (auroral regions excluded)	Constant with latitude at 0.1-7 mbar	[1]
Voyager/IRIS	67°N-72°N	Zonal enhancement by a factor of 9 at 5 mbar in auroral region	[2]
Cassini/CIRS	66°S-71°N (auroral regions excluded)	Decreases toward poles by a factor of 4 at 5 mbar, north-south asymmetry (maximum at 20°N)	[3]
Cassini/CIRS	65°N-85°N	Zonal enhancement by a factor of 6 at 5 mbar in auroral region	[2]
	85°S-70°S	Zonal enhancement by a factor of 3 at 5 mbar in auroral region	
IRTF/TEXES	70°S-70°N	Decreases toward poles by a factor of 2 at 5 mbar, north-south asymmetry (maximum at 20°N)	[4]
IRTF/TEXES	70°S-70°N	Decreases toward poles by factors of 2–3 at 1 mbar, north-south asymmetry decreases over 4 yr of observations	[5]
IRTF/TEXES	45°N-75°N	Zonal enhancement by a factor of 2 at 5 mbar in auroral region	[6]
	80°S-45°S	No significant zonal trend in auroral region	
Juno/UVS	75°S-75°N (auroral regions excluded)	Decreases toward poles by a factor of 2-4 at pressures less than 5–50 mbar	[7]
Juno/UVS	Full coverage	Auroral enhancement by a factor of 2 (north) and 3.5 (south)	[8]
Gemini-N/TEXES	52°N-70°N	Auroral enhancement by a factor of 10-23 at 1 mbar	[9]
	80°S-62°S	Auroral enhancement by a factor of ∼40 at 1 mbar	
JWST/MIRI	55°S-80°S	Auroral enhancement by a factor of 5 at 7 mbar	[10]

thermal structure and hydrocarbon abundances within the southern polar region. They confirmed the earlier findings from Sinclair et al. (2017) on the double-peaked thermal structure, with the two hotpots located at 1 mbar and 0.01 mbar. JWST/MIRI experiences saturation when observing bright bodies, and Rodríguez-Ovalle et al. (2024) developed a specific reduction procedure to desaturate the data and enable the derivation of the C_2H_2 and C_2H_6 abundances. They measured enhancements by factors of ∼5 and ∼7 in the C_2H_2 and C_2H_6 abundances at 7 mbar and 3 mbar, respectively, within the southern polar auroral region (75°S), compared to the region outside the auroral region (60°S).

Tables 1, 2, 3, and 4 summarize the spatially-resolved hydrocarbon measurements including the high-latitude regions. These tables only summarize the observations that led to the derivation of a spatial trend in the hydrocarbon abundances at high-latitudes: either meridional trends, or zonal enhancement at polar auroral latitudes. For a list of prior globally averaged observations, see e.g., Moses et al. (2005a) and Sada et al. (1998). For the corresponding coverage of each of these observing campaigns in terms of latitudinal range observed and pressure levels probed, the reader is referred to Appendix A. Prior studies have derived upper limits for diacetylene (C_4H_2), and propane (C_3H_8), but these are not listed here since no spatial trends were inferred. Note that the acetylene contribution function extents higher in the stratosphere, and also provides abundance information around ∼ 0.1 mbar, though not listed here for the sake of brevity and consistency with the other hydrocarbons.

Table 2 Summary of Jovian ethylene (C_2H_4) measurements. [1] Sinclair et al. (2019) ; [2] Sinclair et al. (2018) ; [3] Sinclair et al. (2023)

Instrument	Coverage	Trend	Ref
Voyager/IRIS	60°N-80°N	Scaling factor of 1.6 in auroral region compared to models	[1]
Cassini/CIRS	65°N-85°N	Scaling factor of 7.2 compared to models	[1]
	85°S-70°S	Scaling factor of 7.2 compared to models	
IRTF/TEXES	45°N-75°N	Zonal enhancement by a factor of 10 at 5 μbar in auroral region	[2]
	80°S-45°S	Zonal enhancement by a factor of 1.7 at 5 μbar in auroral region	
Gemini-N/TEXES	52°N-70°N	Zonal enhancement by a factor of 13 at 1 μbar in auroral region	[3]
	80°S-62°S	Zonal enhancement by a factor of 18 at 1 μbar in auroral region	

Table 3 Summary of Jovian ethane (C_2H_6) measurements. [1] Nixon et al. (2010) ; [2] Sinclair et al. (2017) ; [3] Nixon et al. (2007) ; [4] Fletcher et al. (2016) ; [5] Melin et al. (2018) ; [6] Sinclair et al. (2018) ; [7] Sinclair et al. (2023) ; [8] Rodríguez-Ovalle et al. (2024)

Instrument	Coverage	Trend	Ref
Voyager/IRIS	57°S-56°N (auroral regions excluded)	Increases toward poles by a factor of 2-3 at 5 mbar	[1]
Voyager/IRIS	67°N-72°N	Zonal decrease by a factor of ~2 at 5 mbar in auroral region	[2]
Cassini/CIRS	66°S-71°N (auroral regions excluded)	Increases toward poles by a factor of 1.6 at 5 mbar	[3]
Cassini/CIRS	65°N-85°N	Zonal decrease by a factor of <1.4 at 5 mbar in auroral region	[2]
	85°S-70°S	Zonal decrease by a factor of 1.5 at 5 mbar in auroral region	
IRTF/TEXES	70°S-70°N	Increases toward poles by a factor of 1.5-2 at 5 mbar	[4]
IRTF/TEXES	70°S-70°N	Increases toward poles by factors of 1.8 at 1 mbar	[5]
IRTF/TEXES	45°N-75°N	Lower retrieved concentration within auroral region at <1 mbar, not statistically significant	[6]
	80°S-45°S	Lower retrieved concentration within auroral region at <1 mbar, not statistically significant	
Gemini-N/TEXES	52°N-70°N	Zonal enhancement by a factor of 2-3 at 5 mbar in auroral region	[7]
	80°S-62°S	Zonal enhancement by a factor of 1.8 at 5 mbar in auroral region	
JWST/MIRI	55°S-80°S	Auroral enhancement by a factor of 7 at 3 mbar	[8]

2.1.2 Observational Constraints on the Polar Upper-Atmospheric Mixing Processes

Hydrocarbon mid-IR observations, along with UV-occultation techniques, provide indirect information about the mixing processes controlling the upper atmospheric vertical structure. In the upper stratosphere, the strength of the molecular diffusion increases more rapidly with decreasing pressures than does the eddy diffusion. The species therefore experience a diffusive separation, as their vertical structures become controlled by their own molecular weight above their respective homopause (e.g. Gladstone et al. 1996). Methane, the third most abundant molecule in the lower stratosphere, is well-mixed within the lower to middle stratosphere and its abundance decreases due to molecular diffusion near the homopause and above. The hydrocarbon absorption in specific parts of the far-UV spectrum, combined

Table 4 Summary of Jovian methylacetylene (CH_3C_2H) and benzene (C_6H_6) measurements. [1] Sinclair et al. (2019) [2] Rodríguez-Ovalle et al. (2024)

Instrument	Coverage	Trend	Ref
CH_3C_2H			
Voyager/IRIS	60°N-80°N	Scaling factor of 3.4 in auroral region compared to models	[1]
Cassini/CIRS	65°N-85°N	Scaling factor of <9.6 compared to models	[1]
	85°S-70°S	Scaling factor of 3.4 compared to models	
C_6H_6			
Voyager/IRIS	60°N-80°N	Scaling factor of 15.6 in auroral region compared to models	[1]
Cassini/CIRS	65°N-85°N	Scaling factor of 10.6 compared to models	[1]
	85°S-70°S	Scaling factor of 10.4 compared to models	
JWST/MIRI	55°S-80°S	Auroral enhancement by a factor of 9.7 at 0.5 mbar	[2]

with the sharp decrease in the hydrocarbon concentration above the homopause, allows the derivation of their concentrations using stellar- and solar-occultation techniques.

Several studies discussing the various UV stellar occultations available tend to disagree regarding the derived methane mole fraction at the homopause (see Moses et al. 2005b for a discussion regarding the Voyager-UVS stellar occultation analysis of Festou et al. 1981 and Yelle et al. 1996). The main drawback comes from the limited knowledge of the background atmospheric structure (temperature and wind structures, planetary shape, vertical variation of the mean molecular mass) at the times and locations these occultations are performed. Note that, on Saturn, this situation is slightly better thanks to the simultaneous CIRS and UVIS measurements, allowing the reconstruction with higher precision the atmospheric structure at the location of the stellar occultation (Koskinen and Guerlet 2018; Brown et al. 2024).

Using New-Horizons Alice occultation measurements of χ-Ophiuchus, Greathouse et al. (2010) derived additional values for the eddy diffusion (K_{zz}) coefficient near the methane homopause at two non-auroral latitudes. While the derived value ($3.4^{+9.0}_{-2.8} \times 10^6$ cm^2 s^{-1}) agrees with the previous Voyager-based determination (Festou et al. 1981; Yelle et al. 1996), the corresponding pressure level of the methane homopause differed from these previous determinations. This possibly suggests a change in the strength of the atmospheric mixing.

Despite uncertainty in the derivation of the methane homopause, the range of K_{zz} provided at non-auroral latitude does not seem to agree with those derived in the polar region. Using Cassini-UVIS measurements, Parkinson et al. (2006) could not reproduce the Helium 58.4 nm airglow intensities considering the known eddy diffusion coefficient magnitude derived at lower latitudes. This high-latitude non-solar sources of Helium emission are suspected to be caused by (i) enhanced electron impact, (ii) enhanced vertical mixing, or a combination of both. Parkinson et al. (2006) ruled out (i) using results from the Grodent et al. (2001) polar atmosphere model, suggesting that the eddy diffusion coefficient in the polar mesosphere is enhanced by a factor of 4-10 compared to its lower latitude values.

Using mid-IR infrared observations recorded from IRTF/TEXES, Sinclair et al. (2020) analyzed methane and methyl radical (CH_3) emission spectra measured to further constrain the high-altitude vertical structure in the polar region. Methyl is one of the main methane photolysis by-products, that forms ethane through methyl-methyl recombination. Its abundance is predicted to peak around the methane homopause and is highly dependent on the eddy diffusion coefficient. Initially detected by Cassini-CIRS on Jupiter (Kunde et al. 2004), its emission is optically thin and depends on the upper stratospheric temperature.

Sinclair et al. (2020) tested several photochemical model profiles from Moses and Poppe (2017), considering various assumptions for the eddy diffusion coefficient at pressures less than 10 μbars. Depending on the different model outputs, they produced synthetic spectra for these three molecules by allowing the temperature profile to vary. Sinclair et al. (2020) compared the synthetic emission spectra to the observed ones calculating a goodness-of-fit metric, and concluded that the methane homopause at high-northern latitudes is located at higher altitude. At 62°N, the methane homopause inside the main oval seems located at 461^{+147}_{-39} km above the 1-bar level, i.e. ∼129 km higher than elsewhere (away from the main oval or at lower latitudes). Rodriguez-Ovalle et al. (2023) derived the homopause altitude in the southern polar region from JWST using a similar technique with MIRI observations, suggesting that the methane homopause is located at $\sim 590^{+17}_{-56}$ km above the 1 bar level within the southern main oval. These results seem to disagree with Kim et al. (2017), who found the methane vertical profile in the north polar region relatively similar to the one derived in the equatorial region. This discrepancy is possibly due to the assumed vibrational relaxation rates of methane between these studies (see, e.g., the discussion section of Sinclair et al. 2020), and/or the temporal variability in the studied emissions potentially linked with solar forcing. Indeed, the 8 μm CH_4 emission was previously shown to display daily variability, possibly triggered by solar-wind compressions (Sinclair et al. 2019).

2.1.3 Constraints from Reflected UV Observations

Ultraviolet spectrum of Jupiter in the far-UV carries the absorption signature of several hydrocarbons. Using Cassini-UVIS, Melin et al. (2020) initially derived latitudinal trends for the acetylene and ethane abundance around the low- to mid-latitudes, up to ∼40°. The Ultraviolet Spectrograph (UVS) on Juno similarly provides information on hydrocarbons, as reflected sunlight captured by UVS is partially absorbed by hydrocarbons and haze. The UVS instrument is a photon-counting imaging-spectrograph operating in the 68-210 nm range (Gladstone et al. 2017; Davis et al. 2011; Greathouse et al. 2013). While the primary goal of UVS is to capture the Jovian UV aurora and provide context to Juno's in-situ instruments, it also captures a large amount of non-auroral UV Jovian emissions (Giles et al. 2020, 2021b) and stellar observations (Hue et al. 2019, 2021), due to the spin-stabilized nature of the spacecraft.

Giles et al. (2021a) used Juno-UVS reflected sunlight observations to retrieve the mean C_2H_2 abundance as a function of latitude, excluding the auroral regions. They found a poleward decrease in its abundance by a factor of 2-4 at pressures less than 5-50 mbar, consistent with prior non-auroral mid-IR observations (Nixon et al. 2007; Fletcher et al. 2016; Melin et al. 2018). Giles et al. (2023) then extended this work by analyzing Juno-UVS reflected sunlight maps of Jupiter's poles, including the auroral regions. They compared the mean reflectance at 175-190 nm, where there is absorption from both C_2H_2 and C_6H_6, with the mean reflectance at 190-205 nm, where the absorption from these hydrocarbons is much weaker. Within the main auroral emission, there is a significant enhancement in the 175-190 nm absorption relative to the non-auroral longitudes. This could either be due to an enhancement in the C_2H_2 abundance alone, or due to an enhancement in both C_2H_2 and C_6H_6; variations in C_6H_6 alone cannot reproduce the observations. If the observed variability is entirely due to C_2H_2, Giles et al. (2023) conclude that the C_2H_2 abundance within the auroral oval must be a factor of 3 larger than at similar latitudes but non-auroral longitudes.

Figure 3 compares the C_2H_2 abundance derived in the southern hemisphere with the HCN column density measurements from ALMA (see Sect. 2.3). The contracted and expanded reference ovals displayed are derived from HST UV-observations (Bonfond et al. 2012).

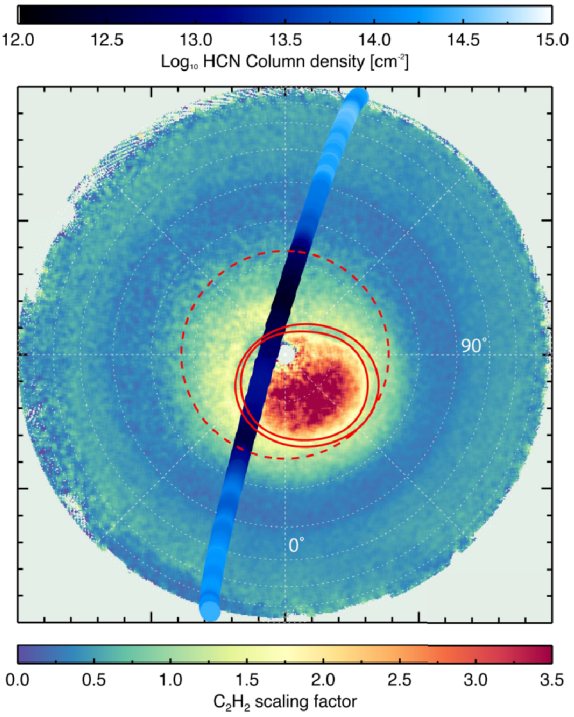

Fig. 3 Southern polar projection of the C_2H_2 abundance derived by Giles et al. (2023) using Juno-UVS reflected sunlight observations. The abundance is expressed as a scaling factor relative to the nominal vertical profile from Moses et al. (2005a). This is compared with the ALMA observations of Cavalié et al. (2023b) who derived the HCN column density at Jupiter's limb (see Sect. 2.3). The contracted and expanded reference ovals derived from HST UV-observations are displayed in solid red/blue lines (Bonfond et al. 2012). The lowest parallel reached by the expanded southern reference oval (67°) is displayed as a dashed circle

The figure also shows the lowest parallel reached by the expanded southern reference oval. Because the aurora is rotating with the planet around the spin axis rather than the magnetic axis, which is significantly tilted with respect to the former, this boundary limits the polar region where the auroral emissions (or auroral-induced chemistry by-products) are most likely to be found.

2.1.4 Summary on Hydrocarbons

All these observations demonstrate that hydrocarbons are locally affected around the polar auroral regions. Mid-IR observations suggest that there is an enhancement in the amount of C_2H_2, C_2H_4, CH_3C_2H, and C_6H_6 at the mbar and sub-mbar levels of the polar auroral regions, i.e., poleward of the main oval. The C_2H_2 auroral enhancement finding was reinforced by a similar conclusion reached using a different wavelength (far-UV), though sensitive to slightly higher pressure level (5–50 mbar). The picture regarding C_2H_6 is less clear. Although earlier Voyager/IRIS and Cassini/CIRS measurements suggest that there is a localized depletion of C_2H_6 at the mbar level in the polar auroral regions, more recent ground-based observations using IRTF/TEXES, Gemini-N/TEXES, or JWST/MIRI show either no statistically significant enhancement of the C_2H_6 abundance, or an increase by a factor of <7 in the auroral regions. Zonally averaged spectra excluding the longitudinal sector containing the aurora however seem to suggest that C_2H_6 is generally enhanced in the polar region compared to the low-to-mid latitudes, as suggested by the Cassini/CIRS measurements retrieved by Nixon et al. (2007, 2010).

2.2 Oxygen Species

The main oxygen species detected in Jupiter's stratosphere are carbon monoxide (CO), water (H_2O), and carbon dioxide (CO_2), ranked according to decreasing abundance. Their stratospheric distributions may result from both internal and external sources, and depend on a balance between vertical and horizontal transport (diffusion and wind), photochemical production/loss processes. Various external sources may supply oxygen species in Jupiter's atmosphere: interplanetary dust particle (IDPs, see Prather et al. 1978), interaction with icy moons and rings (Strobel and Yung 1979), and cometary impacts (Lellouch et al. 1995). Oxygen species can be sourced from the planet's deep interior through upward diffusion of species quenched from deep tropospheric thermochemical equilibrium (Prinn and Barshay 1977; Fegley and Prinn 1988; Yung et al. 1988; Fegley and Lodders 1994; Bézard et al. 2002; Visscher et al. 2010; Cavalié et al. 2023a), though water condenses at the tropopause cold trap. Deciphering the origin of the detected species is achieved through observations spatially resolving these planets (e.g. Lellouch et al. 2006; Cavalié et al. 2013, 2023b), combined with photochemical and thermochemical modeling (Bézard et al. 2002; Lellouch et al. 2002).

2.2.1 Carbon Monoxide

The Jovian stratospheric CO has both an internal and external origin (Bézard et al. 2002). The internal source results from a ∼solar H_2O deep abundance (Li et al. 2020; Cavalié et al. 2023a). In addition, CO was delivered in large quantities by the Shoemaker-Levy 9 (SL9) comet fragments (Lellouch et al. 1997), which impacted Jupiter at several longitudes and around planetocentric latitude of 44°S in July 1994 (Hammel et al. 1995). SL9 deposited CO at pressure levels of ∼0.1 mbar and above. Stratospheric CO appears to have a secondary external source, which was first believed to be the result of more ancient cometary impacts (Bézard et al. 2002), but more likely results from IDP (Moses and Poppe 2017). CO is also produced from CO_2 photolysis, and recycled back into CO_2 through reaction with OH. However, photochemical modeling suggests that CO can be considered as photochemically stable (Moses 1996). Temporal evolution of its spatial distribution several years following the SL9 impact allowed the derivation of the total mass of CO brought into the atmosphere as well as the vertical and horizontal diffusion coefficients (Bézard et al. 2002; Moreno et al. 2003).

About 22.5 years after the SL9 impact, ALMA measured the CO abundance at Jupiter's limb (Cavalié et al. 2023b). Spectral inversion indicated a rather latitudinally uniform CO column density of $1.86 \pm 0.52 \times 10^{16}$ cm^{-2} (see Fig. 4, top panel). This corresponds to a loss factor of 0.9 ± 0.3 since the measurements of Moreno et al. (2003) recorded between 1995 and 1998 using the JCMT 15m and IRAM 30m telescopes.

2.2.2 Water

Condensation generally prevents H_2O from diffusing from the troposphere to the stratosphere of Jupiter, while spurious storm outbreaks may periodically overshoot the tropopause cold trap (Sánchez-Lavega et al. 2008). Water was directly detected in the atmosphere following the SL9 impact (Bjoraker et al. 1996; Encrenaz et al. 1997). Measurements 3 years after the impact using ISO indicated that stratospheric water was restricted to pressure levels $p < 0.5 \pm 0.2$ mbar. This was interpreted as a strong indication that the stratospheric water resulted directly from SL9 and subsequent chemistry (Lellouch et al. 2002).

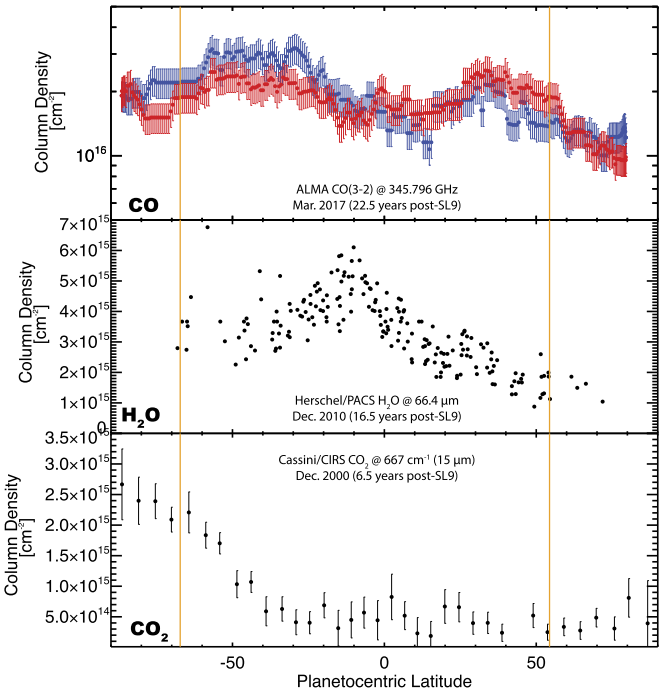

Fig. 4 Top panel: meridional CO column density derived from the CO (3-2) line observed by ALMA on 22 March 2017 at Jupiter eastern (red) and western (blue) limb. Adapted from Cavalié et al. (2023b). Middle panel: meridional H_2O column density derived from Herschel/PACS observations at 66.4 μm on 15 December 2010. Adapted from Cavalié et al. (2013). Bottom panel: meridional CO_2 column density derived from Cassini/CIRS observations at 667 cm^{-1} on December 2000. Adapted from Lellouch et al. (2006)

Observations from the Submillimeter Wave Astronomy Satellite (SWAS) as well as early Odin disk-averaged observations lacked the sensitivity to further constrain the external source of H_2O (Bergin et al. 2000; Cavalié et al. 2008). However, the Odin space telescope provided long-term monitoring of the globally-averaged stratospheric water, which tended to confirm the cometary origin of H_2O (Cavalié et al. 2012; Benmahi et al. 2020).

The strongest evidence for the origin of water in Jupiter's stratosphere came from Herschel HIFI (Heterodyne Instrument for the Far Infrared) and PACS (Photodetector Array Camera and Spectrometer) observations. Disk-resolved mapping of the water emission at 66.4 μm showed a factor of 2-3 decrease in the water column density from the southern to the northern hemisphere (Cavalié et al. 2013). Meridional cross-sections of the column density derived from the Herschel/PACS observations are shown on Fig. 4, and compared with other oxygen species. The peak in the water column density around 15°S likely results from a localized warmer temperature observed at this latitude that was not accounted for in the spectral modeling.

Over the years, the water emission line was expected to become fainter, as water diffused horizontally across Jupiter's disk, and more broadly, as the SL9-related stratospheric water diffused down to higher pressure levels. Benmahi et al. (2020) showed that the line-to-continuum ratio indeed decreased by ∼40% between 2002 and 2019, and that the H_2O cutoff level migrated downwards from 0.2 mbar in 2002 to 5 mbar in 2019. Photochemical models can reproduce such a decrease provided that the efficiency of the vertical eddy diffusion

coefficient increases in this pressure range. This in turns degrades the model agreement with the observed hydrocarbons, suggesting that an additional process might be responsible for the water loss. Benmahi et al. (2020) suggested that auroral chemistry may be the reason for this additional loss through ion-neutral chemistry triggered by electron precipitation.

2.2.3 Carbon Dioxide

The situation for CO_2 is not as straightforward since it can be created from H_2O photolysis and subsequent reaction with CO, which has a time-variable spatial distribution. Disk-resolved ISO observations initially indicated latitudinal variations, with a factor of ∼7 decrease in its column density from southern mid-latitudes to northern mid-latitudes (Lellouch et al. 2002). The ISO spatial resolution was however modest, only providing a couple of resolution elements across Jupiter.

The Cassini flyby of Jupiter provided higher spatial resolution observations, showing a strong CO_2 column density peak around the south pole (Kunde et al. 2004; Lellouch et al. 2006). Reconciling both the meridional distribution of CO_2 with the known post-SL9 distributions of H_2O and CO was a challenge. While minor CO_2 polar excess could be interpreted as a combination of the water photolysis by-product (OH) reacting with carbon monoxide, the observed magnitude of the CO_2 polar excess requires a different explanation. Magnetosphere-ionosphere coupling provides a means to locally supply ions originating from Io into the polar region, though the required quantity of oxygen ions to explain the CO_2 spatial distribution was unrealistically large (Lellouch et al. 2006). Finally, the CO_2 polar excess was explained using a combination of meridional diffusion combined with a poleward advection (discussed in Sect. 3), though it has remained not a fully satisfactory solution given the transport constraints resulting from the HCN distribution measured simultaneously (see next section).

The CO, H_2O, and CO_2 meridional column densities have been measured at different post-SL9 times, which makes it difficult to find a unique interpretation. The measurements are summarized on Fig. 4. Over-plotted in orange are the delimitation of Jupiter's auroral regions, defined here as the lowest parallels reached by the expanded reference ovals (Bonfond et al. 2012). This corresponds to 54°N and 67°S.

2.3 Nitrogen Species

The only N-bearing species detected in Jupiter's stratosphere is HCN, while NH_3 is detected at pressures greater that ∼100 mbar. Observations prior to the SL9 impact debated whether HCN was already present in the stratosphere in measurable quantities (Tokunaga et al. 1981; Bézard et al. 1995), and Bézard et al. (1995) only derived a mole fraction upper limit of 8×10^{-10} at p<55 mbar. HCN was later observed in large quantities in Jupiter's stratosphere in the aftermath of the SL9 impact, with a total mass of HCN of 6×10^{11} g on one well-studied impact fragment (Marten et al. 1995).

While most HCN directly derives from impact-induced shock-chemistry (Zahnle 1996), additional post-impact production resulted from the photolysis of NH_3 transported from the troposphere to the stratosphere during the impacts (Griffith et al. 1997; Moses et al. 1995). Temporal changes of its distribution during the years following the impact are mostly related to mixing processes (e.g., vertical and horizontal diffusions). This makes HCN an important species for tracing the Jovian dynamics in a region otherwise devoid of obvious tracers such as clouds. Monitoring its distribution up to 4 years after the impacts provided valuable information regarding the efficiency of the horizontal mixing (Moreno et al. 2003; Griffith et al. 2004), as discussed in Sect. 3.

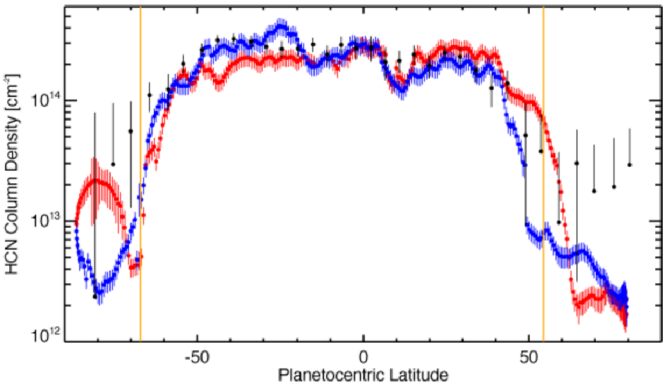

Fig. 5 HCN column density derived from ALMA at the eastern (red) and western (blue) limbs observed on in March 2017 (22.5 years post-SL9) (Cavalié et al. 2023b). It is compared with the CIRS-derived HCN column density in December 2000 (6.5 years post-SL9) shown in black (Lellouch et al. 2006) and divided by a factor of 10. The vertical orange lines represent the boundary of the auroral regions

Similar to CO_2, the Cassini flyby provided more complete latitudinal coverage of the HCN column density than that provided by the observations of Griffith et al. (2004), and at higher spatial resolution than observations of Moreno et al. (2003). The Cassini-CIRS observations measured the HCN column density as a function of latitude 6.5 years post SL9 (Lellouch et al. 2006). Not only did it allow estimation of the strength of the vertical and meridional mixing, but it also revealed a sharp drop by a factor ∼7 from the SL9 impact latitude to the south polar region. This drop was hard to reconcile with the CO_2 polar excess, given the simultaneity of these observations, combined with the fact that both species were presumed to derive from the SL9 impact. The conclusion was that the HCN distribution could be explained assuming a sharp cutoff in the meridional eddy mixing coefficient (over an order of magnitude) poleward of 40°S combined with equatorward advective transport. The markedly different distribution of CO_2 and HCN led Lellouch et al. (2006) to conclude that they likely resided at different pressure levels (5-10 mbar and 0.5 mbar, respectively), and therefore implying very different horizontal transport regimes.

ALMA observations recorded in March 2017 provided another measure of the HCN meridional distribution 22.5 years after the SL9 impact (Cavalié et al. 2023b), shown here on Fig. 5. Thanks to ALMA's high-spectral resolution, one notable feature from this dataset was the strikingly different lineshape of the HCN (4-3) emission line between the high- and low-latitude regions. This indicates that the vertical distribution of HCN is different between these two regions, with HCN residing at $p < 0.1$ mbar in the auroral regions, and $p < 3$ mbar at lower latitudes.

Two additional striking features were also discovered in the ALMA dataset from Cavalié et al. (2023b). First is the factor of 10 higher HCN column density observed at 75°S–85°S, around 350°W compared to the other measurements at nearby latitudes, and interpreted as a high-altitude HCN production source within the auroral regions. Second is the almost 2 orders of magnitude drop in the HCN column density above both poles compared to the low latitudes, that they interpreted as a result from heterogeneous chemistry with stratospheric aerosols, and which will be discussed in Sect. 2.5.

2.4 Ions

The only ion detected in Jupiter's atmosphere is H_3^+, first discovered by Drossart et al. (1989). Charged particle precipitations in the upper atmosphere of Jupiter lead to the formation of H_2^+ through electron impact ionization $H_2 + e^- \rightarrow H_2^+ + 2\,e^-$. This light ion then reacts with molecular hydrogen to form H_3^+ through the reaction:

$$H_2^+ + H_2 \rightarrow H_3^+ + H \tag{1}$$

H_3^+ produces emission lines in the near-IR, which allows the ionosphere of Jupiter to be sounded. The emission lines can be inverted using radiative transfer calculations to derive H_3^+ temperature and number density, assuming the ion is in quasi-local thermodynamical equilibrium (LTE) (see, e.g., the review of Badman et al. 2015). This ion number density peaks around the auroral regions and decreases towards lower latitudes along with this species' temperature, showing it plays an important role in controlling the upper atmospheric temperature of Jupiter (O'Donoghue et al. 2021).

H_3^+ is lost through dissociative recombination above the methane homopause. The lifetime of the H_3^+ electron recombination is given by $\tau_r = (k_r\ n_e)^{-1}$, where k_r is the recombination rate constant and n_e the electron density (Achilleos et al. 1998). In the auroral region, the electron densities derived from the Voyager 2 radio occultation measurement at 66°S, 258°W range from $\sim 5\times10^4$ to 3×10^5 cm^{-3} in the 600-1200 km altitude range (Hinson et al. 1998), i.e., where the H_3^+ emission peak occurs (Tao et al. 2011). Using the formula for $k_r = 1.15 \times 10^{-7}\ (300/T)^{0.65}$ cm^3 s^{-1} from Sundstrom et al. (1994), this leads to an H_3^+ lifetime in the 20-300 s range. This lifetime is orders of magnitude shorter than the lifetime of the neutral chemical species discussed in this paper, and therefore measurements of the H_3^+ distribution can only be used to trace dynamical processes over a relatively short timescale, as discussed in Sect. 4.

Note that, below the methane homopause, H_3^+ is also destroyed through reaction with CH_4 ($H_3^+ + CH_4 \rightarrow CH_4^+ + H_2$) and heavier hydrocarbons, such as C_2H_2, C_2H_4, and C_2H_6 (Kim and Fox 1994), as detailed in Sect. 3.2.

2.5 Aerosols and Hazes

The term hazes has been historically used to define layers of sub micron-sized particles located in the upper troposphere (200-500 mbar), as well as stratospheric particles located at pressures lower than 100 mbar, while the term cloud refers to larger-sized condensates composing the more variable layers seen in the visible at higher pressure levels (see reviews of West et al. 1986, 2004).

Some of the most striking high-latitude features at Jupiter's poles include a near-UV dark polar cap, and the bright polar hood as seen in near-IR methane band imagery (e.g. West et al. 2004, and references therein), from which the aerosol distribution, size and shape can be constrained using observations at multiple phase angles. Figure 6 shows snapshots of the bright polar hoods in a strong methane absorption band at 2.1 μm, as captured by JWST/NIRCam (Hueso et al. 2023). The hazes are more optically thick in the south hemisphere than in the north. In both hemispheres, the latitudinal distributions of the lower stratospheric hazes are constrained by defined boundaries showing a complex wave structure consistent with Rossby waves (Sanchez-Lavega et al. 1998; Barrado-Izagirre et al. 2008), and JunoCam provided some of the most spatially-resolved observations of this wave pattern to date (Rogers et al. 2022).

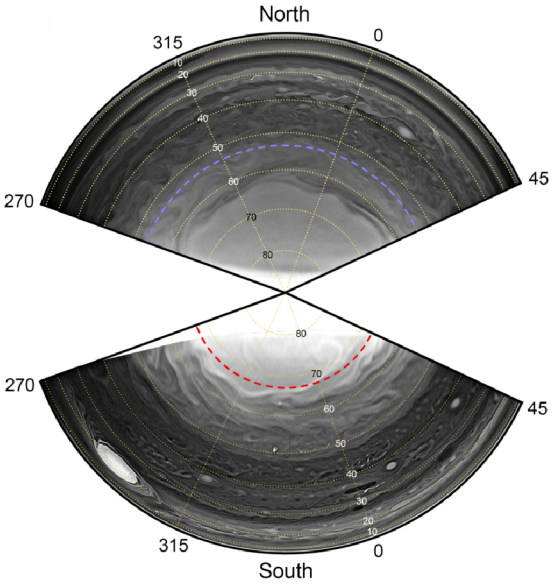

Fig. 6 Composite image of James Webb Space Telescope observations of Jupiter in a narrow 2.12 μm filter (F212N; data from Hueso et al. 2023). The image has been contrast-enhanced and high-pass filtered to show the complex details present in the hazes. Following Fig. 3, red/blue dashed lines in the southern/northern hemisphere show the lowest parallel reached by the expanded auroral reference ovals

Cloud structure and formation, as well as upper tropospheric haze layers will not be discussed here, as the focus of this paper is on the distribution of stratospheric species with an emphasis on the polar regions. However, we refer the reader to the work of Wong et al. (2020) that serves as a reference to the observing campaigns performed simultaneously to the Juno mission from 2016-2019, in the UV/Visible/near-IR, providing information on the upper-tropospheric wind field, as well as cloud structure and distribution.

Pryor and Hord (1991) used observations from the Voyager 2 Photopolarimeter Subsystem (PPS) to characterize and provide an explanation for Jupiter's UV-dark polar cap, previously discovered by Hord et al. (1979). They compared the location where this behavior was observed with Jupiter's auroral zone, and suggested that ion-neutral chemistry would lead to the destruction of methane, and ultimately promote the creation of haze through the production of large hydrocarbons.

Kim et al. (1991) used spectroscopic observations in the broad 2-μm methane absorption band to constrain the altitudes of the polar hazes to pressure levels from 70 to 5 mbar. Sanchez-Lavega et al. (1998) used HST and Voyager observations in the UV and methane absorption band at 890 nm to characterize the polar stratospheric hazes, showing that the hazes are located at around 100 mbar and are latitudinally limited by Rossby waves that interact with the zonal jets at the troposphere. Vincent et al. (2000) used HST observations in the UV to study the polar stratospheric aerosols at pressures of few tens of mbar, finding evidence of weak westward motions in the range of -3 to -11 m s^{-1} and meridional mixing in the polar stratosphere.

Rages et al. (1999) used Galileo observations recorded by its Solid State Imaging subsystem (SSI) in the violet ($\sim$417 nm) and near-IR ($\sim$756 nm) to study the stratospheric hazes. The SSI violet observations are sensitive to the particle properties around the 20 mbar pressure region and above. They retrieved stratospheric aerosol particles with sub-micron sizes, and haze number densities increasing by one order of magnitude from low- to high-latitudes. They also obtained an alternative solution at high latitude, with particle sizes in the 1.3 μm range.

The Cassini/ISS instrument provided images of Jupiter through several filters at a wide range of phase angles. Some of the filters of interest for this present paper are the UV1 (0.258 μm), MT3 (0.889 μm) and CB3 (0.938 μm) filters. The UV1 filter probes the lower stratosphere due to Rayleigh scattering being the main opacity source. Methane absorption is the main opacity source in the wavelength region covered by the MT3 filter which probes the lower stratosphere, while CB3 is a continuum filter centered around the methane window (Porco et al. 2003, 2004). These observations resulted in detailed maps of the polar aerosols (Barrado-Izagirre et al. 2008), and showed the formation and later evolution and dispersal of a large dark oval inside the north auroral oval probably associated with an auroral event (Barbara et al. 2024).

Several additional studies have attempted to produce detailed retrievals of the properties of the polar stratospheric aerosols. Post-SL9 observations in the near-IR H (1.45-1.8μm) and K (1.95-2.5μm) bands were previously used to retrieve the aerosol properties and distribution on Jupiter (Banfield et al. 1996). Using this inversion method, Banfield et al. (1998) extended the retrieval to a larger range of latitudes. They calculated the location of the haze layer at low-latitudes to be $\sim$50 mbar while, in the polar region, their location was estimated to be $\sim$20 mbar. Some of the assumptions made in these works include holding the aerosol particle size constant (0.3 μm), i.e., within the particle size range of 0.2-0.5μm, as previously constrained using near-UV observations (Tomasko et al. 1986).

While the 0.3 μm-size aerosols provide a good fit of the near-IR at low-latitudes, reproduction of the 1.7-1.75 μm and 2.05-2.1 μm ranges at high latitude proved more challenging (Banfield et al. 1998). Using a similar method to Banfield et al. (1996, 1998), Zhang et al. (2013) relaxed the constraints on the aerosol particle size and demonstrated that the high-latitude spectra were better fit when considering 0.7 μm-radius aerosols. Zhang et al. (2013) also improved the method from Banfield et al. (1996) by using refined CH_4 absorption coefficients from Karkoschka and Tomasko (2010), which slightly shifts to higher pressure levels the aerosol layer compared to the work of Banfield et al. (1998). The inferred stratospheric aerosol map of Zhang et al. (2013) displayed a dichotomy between mid- and high-latitude. At low- to mid-latitudes, stratospheric aerosols are located within 1-2 scale heights near 50 mbar, while they are above 20 mbar at higher latitudes.

By combining ground-based near-IR observations and the Cassini/ISS limb-darkening observations at multiple phase angles, Zhang et al. (2013) were able to derive an aerosol density map. They tested two properties of aerosols; one consisting of compact sub-micron particles, and the other consisting of fractal aggregates composed of small monomers. While the scattering properties of compact sub-micron particles are best reproduced using Mie theory, additional phase functions (e.g., Henyey-Greenstein) are needed for larger particles. They conclude that two types of particles are needed to explain the UV1 and MT3 limb-darkening profiles recorded at multiple phase angles. The low-latitude (40°S-25°N) images are best fit using compact sub-micron particles, with sizes in the 0.2-0.5μm range. The high-latitude regions are best fit assuming fractal aggregate particles consisting of thousands of $\sim$10 nm monomers. The derived aerosol column density is $\sim$2 orders of magnitude greater in the polar versus the low-latitude regions. While they noted the non-uniqueness of their solution, they provided the possible range of monomer size and number depending on the assumed imaginary part of the UV refractive index. Figure 7 shows the aerosol distribution map retrieved by Zhang et al. (2013).

Heterogeneous chemistry on aerosols may affect the chemical distribution of several species. Laboratory experiments found that HCN bonds with aerosols once they reach a typical size of $\sim$0.1 μm (Perrin et al. 2021). Such sized aerosols are predicted to be present in Jupiter's polar regions around the $\sim$mbar level from observations (Zhang et al. 2013),

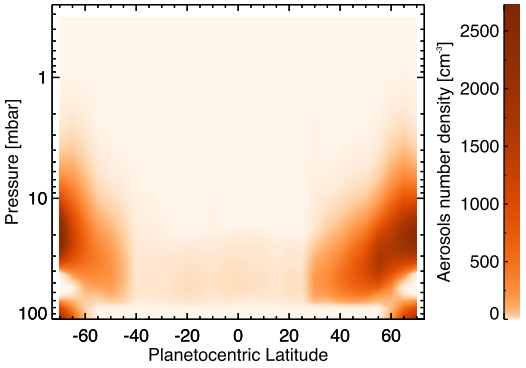

Fig. 7 Zonally-averaged aerosol map (cm^{-3}) derived from ground-based near-IR observations and Cassini/ISS observations from Zhang et al. (2013)

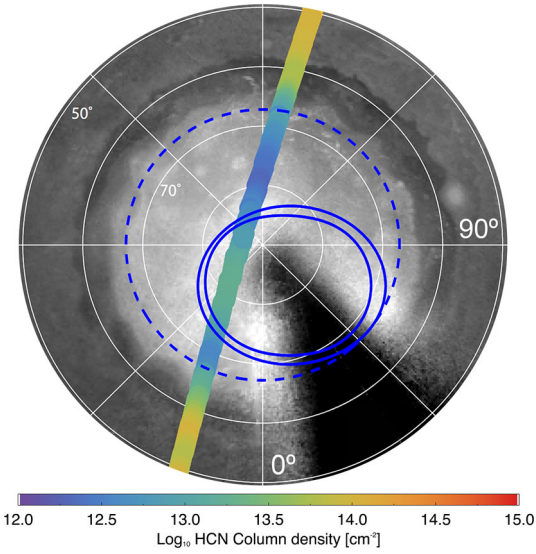

Fig. 8 Composite image of the methane-filter image of Jupiter's south polar region from JunoCam (Rogers et al. 2022) recorded during Juno PJ24, and compared with the HCN column density using ALMA derived by Cavalié et al. (2023b). The contracted and expanded reference auroral ovals derived from HST observations are displayed in solid blue line (Bonfond et al. 2012). The lowest parallel reached by the expanded southern reference oval (67°S) is displayed as a dashed circle

and modeling work (Friedson et al. 2002), as will be described in Sect. 3. Figure 8 compares the methane-band image of the JunoCam experiment (Hansen et al. 2017), with the HCN column density derived by Cavalié et al. (2023b). In the absence of clouds, JunoCam methane-filter images probe a pressure level of 540 mbar, as determined from the $\tau = 1$ optical depth at 889 nm from Sánchez-Lavega et al. (2013), and higher in the stratosphere in the presence of clouds, and may be used as a proxy for the aerosol distribution. The striking spatial correlations between the HCN depletion in the region of enhanced hydrocarbon production near the auroral region (Fig. 3) and polar aerosols (Fig. 8) favor the scenario where HCN is depleted from heterogeneous chemistry, although more experimental work is needed to constrain the heterogeneous chemical reactions involved.

Reviews of several relevant models aiming at explaining the observed chemical distributions are now summarized.

3 Atmospheric Models

3.1 Neutral Photochemical Models

Methane photolysis and its consequence on stratospheric chemistry caught the interest of the community several decades ago (Cadle 1962; Strobel 1969, 1973). In the mid-IR, hydrocarbons are detected in the mbar and sub-mbar levels. In these regions, their abundances are controlled by a combination of chemical reactions triggered by the by-products of methane photolysis and subsequent chemistry, combined with downward diffusion as well as horizontal mixing.

Allen et al. (1981) initially developed the Caltech/JPL 1D photochemical and transport Model (KINETICS), which was further refined later (Yung et al. 1984; Gladstone et al. 1996; Moses et al. 2000, 2005a). Alternatively, Dobrijevic and Parisot (1998) developed a photochemical model for the giant planets, not only to interpret ground- and space-based observations, but also to study the sensitivity of the model output to uncertainties in the chemical reaction rates (Dobrijevic et al. 2003, 2010, 2011).

Photochemical and thermochemical models allow the in-depth study of the chemical inventory in planetary atmospheres. Unlike general circulation models, photo-/thermochemical models are restricted to solving the continuity equation for a set of non-linearly coupled equations, each equation representing the temporal evolution of a given individual species. This allows exploring the complexity of the chemical network, despite having simplified transport processes. Because several hydrocarbons were detected early on, these models initially focused on reproducing the hydrocarbon distributions.

One-dimensional (altitude) photochemical models were first developed to interpret the early observations of the outer planets, since such observations were mostly disk-averaged, or with a handful of resolution elements. Such models would generally solve i continuity equations (2), non-linearly coupled by a set of m reactions:

$$\frac{\partial n_i}{\partial t} = P_i - n_i L_i - \frac{\partial \Phi_i}{\partial z} \tag{2}$$

where n_i, z, P_i, L_i, and Φ_i represent the abundance of species i, the altitude, the chemical production term of species i, the chemical loss term of species i, and the vertical flux of species i, respectively. Depending on the number of species considered and the extent of the network, i generally ranges from a few dozen to several hundred, while m can be up to several thousand.

The observations gathered by missions such as Cassini-Huygens, or the constantly increasing ground-based capabilities provided the abundance distribution of certain species as a function of latitude, longitude and season, therefore challenging the predictive capabilities of uncoupled 1D-models covering different latitudes. Using Saturn as an illustration, Moses and Greathouse (2005) first developed a seasonal model of Saturn's stratosphere, consisting of a series of 1D-models, in order to interpret the IRTF/TEXES mid-IR observations of Saturn (Greathouse et al. 2005). They showed that the meridional trend of C_2H_2 was fairly well reproduced by the model, characterized by a meridional decrease in its abundance from equator to higher latitudes, thus following the yearly average of solar illumination. However, their predicted C_2H_6 meridional trend was anti-correlated with the observations, likely due to the higher sensitivity of C_2H_6 to transport processes because of its longer chemical lifetime.

Cassini-Huygens arrived at Saturn in July 2004, and the CIRS instrument provided a comprehensive dataset of nadir- and limb-sounding measurements of Saturn's main hydrocarbons at different latitudes and over half a Kronian year (Flasar et al. 2005; Howett

et al. 2007; Guerlet et al. 2009, 2010; Sinclair et al. 2013; Sylvestre et al. 2015). To interpret these observations, Hue et al. (2015, 2016) developed a seasonal 2D-photochemical (altitude-latitude) model that calculates the seasonal variation of abundances, first by turning the meridional diffusion off. Essentially, the set of equations solved in a 2D-photochemical model (see Eq. 3) is similar to the 1D model:

$$\frac{\partial n_i}{\partial t} = P_i - n_i\, L_i - \frac{1}{r^2}\frac{\partial (r^2 \Phi_i^r)}{\partial r} + \frac{1}{r\cos\theta}\frac{\partial (\cos\theta \Phi_i^\theta)}{\partial \theta} \tag{3}$$

where r, θ, Φ_i^r, Φ_i^θ represent the radial direction, the latitude, the vertical flux of species i, and the meridional flux of species θ, respectively.

Cassini/CIRS limb-sounding measurements on Saturn were reasonably well-reproduced from the equator up to ±40° in the 0.1-1 mbar range. Deviation from the model prediction beyond 40°S indicates large-scale stratospheric dynamics (Hue et al. 2015). Some of the main takeaway from the Moses and Greathouse (2005) and Hue et al. (2015) studies is that photochemistry controls the abundance distribution of the C_2H_x, and that the deeper in the stratosphere the more they are controlled by the annually-averaged insolation instead of the instantaneous insolation. The predicted seasonal variability in the C_2H_x molecules are only noticeable at pressures lower than 0.1 mbar.

On Jupiter, the situation is different due to its lower obliquity, making seasonal effects more muted than on Saturn. Liang et al. (2005) developed a quasi-two-dimensional model to study the effect of meridional diffusion on the hydrocarbon meridional distributions from Cassini/CIRS (Kunde et al. 2004). They coupled the 1D results from KINETICS with a meridional diffusion coefficient, K_{yy}, and inferred a $K_{yy} \sim 10^{11}$ cm^2 s^{-1} above the 10 mbar level, and $K_{yy} \leq 10^9$ cm^2 s^{-1} below the 5-10 mbar pressure level, in agreement with post-SL9 dust tracking, though about two orders of magnitude smaller than values derived from tracking post-SL9 stratospheric chemical species (Moreno et al. 2003; Griffith et al. 2004; Lellouch et al. 2006).

Diffusion models have been developed to interpret the post-SL9 species, bringing constraints on diffusive processes occurring in Jupiter's stratosphere. Horizontal diffusion models have been developed to understand the latitudinal spread of the post-SL9 species such as HCN, CO, CS (Moreno et al. 2003; Griffith et al. 2004), providing an estimate of the K_{yy} magnitude. Such approaches assume that the vertical diffusion timescale is longer than the horizontal one, and that these species are chemically stable, which are both reasonable assumptions (Moses et al. 1995).

Lellouch et al. (2006) expanded upon this approach and modelled the distribution of HCN and CO_2 (see Figs. 4 and 5) including a meridionally variable K_{yy} and meridional winds v_θ. They used an inversion technique to derive the optimal parameter $K_{yy}(\theta)$ first by only assuming meridional diffusion, and then by adding advective transport. Considering HCN first, they added a HCN chemical production term, deriving from the NH_3 photolysis. They concluded that (i) HCN production from NH_3 is negligible in controlling its meridional distribution, (ii) equatorward winds are needed to reproduce the HCN observations. They proceeded with modeling the CO_2 distribution, while accounting for the relevant chemical species and reactions involved in the production and destruction of CO_2, based on Lellouch et al. (2002). They were successful at reproducing the CO_2 polar enhancement assuming meridionally uniform K_{yy} combined with a poleward advective transport. The difference in the advective transport needed to reproduce HCN (equatorward transport) and CO_2 (poleward transport) was interpreted as an indication that both species resided at different pressure levels, i.e., 5-10 mbar for CO_2 and 0.5 mbar for HCN (as discussed in Sect. 2.3).

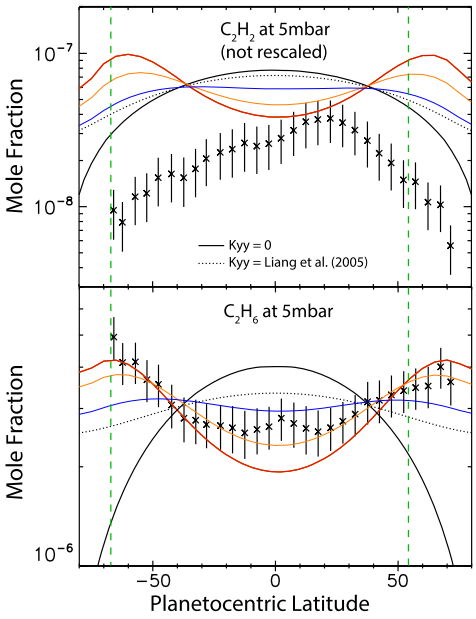

Fig. 9 Meridional distribution of C_2H_2 and C_2H_6 abundances at 5 mbar from Hue et al. (2018). Black solid line: photochemical predictions with $K_{yy} = 0$. Black dotted line: photochemical predictions with K_{yy} taken from Liang et al. (2005). Red/blue/orange lines: photochemical predictions with K_{yy} taken from Liang et al. (2005) and stratospheric 2D advective transport. The model results are compared with the Cassini/CIRS observations of Jupiter (Nixon et al. 2010). The lowest parallels reached by the expanded reference ovals are displayed as vertical dashed green lines. Figure adapted from Hue et al. (2018)

Hue et al. (2018) adapted a version of their Saturn seasonal model to Jupiter in order to compare their results with the hydrocarbon measurements retrieved from the Cassini/CIRS observations (Nixon et al. 2010). The use of a 2D model allows the addition of K_{yy} as well as 2D wind patterns. The meridional distributions of C_2H_2 and C_2H_6 measured by Cassini/CIRS were compared to the model output, while considering the following number of cases:

- $K_{yy} = 0$ (equivalent to a sum of 1D models run at different latitudes),
- $K_{yy} \neq 0$ (using constraints from post-SL9 chemical species tracking of Lellouch et al. 2002; Moreno et al. 2003; Griffith et al. 2004; Lellouch et al. 2006),
- $K_{yy} \neq 0$ and advective circulation (winds).

Results of a 2D-photochemical model that assumes a constant K_{yy} with altitude ($K_{yy} = 2 \times 10^{11}$ cm^2 s^{-1}), combined with a two-cell circulation pattern are shown in Fig. 9, taken from Hue et al. (2018). The circulation cells were parameterized assuming upwelling winds at low-latitudes ($<30°$) and downwelling winds at higher latitudes. The two nodes of the cells were arbitrarily fixed at $\pm 30°$, as a numerical experiment, in order to demonstrate the interplay between the strength of the advective (winds) and diffusive (K_{yy}) transport in controlling the meridional distribution of hydrocarbons. Hue et al. (2018) used constraints from Lellouch et al. (2006) to build their 2D-wind field. Lellouch et al. (2006) assumed a sinusoidal variation in the amplitude of the latitudinal winds, with maximum winds at $\pm 45°$ latitude and zero at the equator and the poles (see their Fig. 7). In the southern hemisphere at $\pm 45°$ latitude, they assumed winds of 7-9 cm s^{-1} at $\sim$ 0.5 mbar towards the equator, and winds of 30 cm s^{-1} in the direction of the poles at $\sim$ 5-10 mbar to reproduce the HCN and CO_2 distribution, respectively.

Hue et al. (2018) showed that, in order to reproduce the 5 mbar C_2H_6 meridional trend measured by Cassini/CIRS, a circulation cell flowing in the opposite direction, i.e., with upwelling motions at the equator and downwelling motion at higher latitude, was needed. Model outputs are displayed on Figs. 9 and 10, and compared with the Cassini/CIRS measurements from Nixon et al. (2010). Fig. 9 shows that while the C_2H_2 meridional gradient

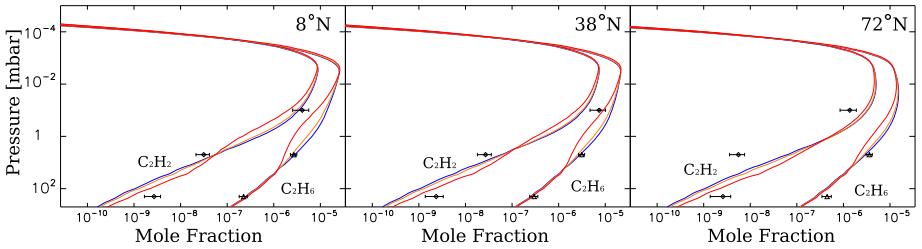

Fig. 10 Vertical profiles of C_2H_2 and C_2H_6 at 8N (left panel), 38N (middle panel) and 72N (right panel). The vertical profiles are only presented when the stratospheric circulation is added to the photochemical model. The corresponding wind velocities are presented on Fig. 9 of Hue et al. (2018). The model results are compared to the Cassini/CIRS observations of Jupiter at 0.1 mbar (C_2H_2 only), 5 mbar and 200 mbar Nixon et al. (2010). Image reproduced with permission from Hue et al. (2018), copyright by Elsevier

can be reproduced using $K_{yy} = 0$ and no winds (solid line), the meridional distribution of C_2H_6 is however best reproduced, in terms of equator-to-pole gradients, using a combination of moderate meridional diffusion coefficient ($K_{yy} \neq 0$) with a circulation cell with upwelling motions at the equator and downwelling motions at mid-latitudes. Alternatively, implementing in the 2D-photochemical model a circulation cell using loose constraints suggested by Lellouch et al. (2006) reinforces the equator-to-pole C_2H_2 meridional gradient, but degrades at the same time the model/observation agreement for C_2H_6.

Compared to Earth's atmospheric circulation, the understanding of transport mechanisms in Jupiter's stratosphere is limited. Voyager/IRIS performed the first spatially resolved measurements of the latitudinal distributions of wind and temperature. These measurements allowed Gierasch et al. (1986) to deduce the existence of a circulation in the upper troposphere, using an axisymmetric model that accounts for perturbations in the zonal wind and thermal fields. Conrath et al. (1990) extended this study by including radiative forcing and extending the calculation to the stratosphere. In the stratosphere, the predicted meridional circulation turns into two large cells with upwelling at the equator and downwelling at the poles. However, their calculations did not account for atmospheric aerosols.

West et al. (1992) and Moreno and Sedano (1997) demonstrated that including aerosols, with different distributions, may lead to opposite circulation patterns in the stratosphere, suggesting the atmospheric circulation is highly sensitive to the aerosol properties. Guerlet et al. (2020) and Zube et al. (2021) highlighted the critical role of assumed aerosol distributions in controlling the Jovian stratospheric radiative budget and circulation patterns. Guerlet et al. (2020) found that, at pressure less than 3 mbar, the predicted circulation is independent of aerosol assumptions, with upwelling motions near the equator and downwelling poleward of 50°. In the lower stratosphere, the predicted circulation of Guerlet et al. (2020) varies with the considered aerosol scenarios, and the predicted circulation with their most realistic scenario would be generally inconsistent with the *ad hoc* circulation implemented by Hue et al. (2018) to reproduce the Cassini/CIRS observations.

Because C_2H_2 and C_2H_6 are chemically coupled and have lifetimes of the same order of magnitude, Hue et al. (2018) showed that no combination of diffusion coefficients (K_{zz} and K_{yy}) with a circulation pattern can explain the meridional distributions CIRS recorded. A alternative way to produce radically different meridional distributions for these two compounds would be to invoke a (photo-)chemical process that would be strongly coupled to only one of them. Ion-neutral chemistry could be a good candidate, and will be discussed in the next section. However, one should note that the retrieval performed on the Cassini/CIRS

observations by Nixon et al. (2007, 2010) excluded the longitudinal range around the auroral region.

3.2 Ion-Neutral Photochemical Models, and Aerosol Formation Models

Kim and Fox (1994) initially calculated the effect of photo-ionization on the hydrocarbon ion chemistry. The ionization produces secondary electrons which, in turn, can ionize, dissociate and excite atmospheric gases. They developed an atmospheric model separated into two regions, (i) the ionosphere above 700 km (2×10^{-6} mbar), where only light ions containing H and He atoms were included, as well as atomic hydrogen, and (ii) the lower ionosphere below 700 km, where hydrocarbons up to two carbons were included, and pseudoions for the C_3H_x and C_4H_x. Note that Kim and Fox (1994) are using the 0.6 bar ammonia cloud top as the z = 0 km reference altitude. We have added the corresponding atmospheric pressure associated with each result from their paper. The lower ionospheric model solves the continuity equation for 21 ions and 12 neutrals. The abundances of CH_4, C_2H_2, and C_2H_6 at the lower boundary of the lower ionospheric model were set consistently according to Voyager UV occultation data, while the abundances of CH_3 and C_2H_4 were set according to photochemical model calculations from Gladstone et al. (1996). The two models were solved iteratively and the results at the common boundary (700 km) were fed into each other until convergence was reached.

Kim and Fox (1994) predicted the formation of a hydrocarbon ion layer around 270-470 km altitude ($\sim 10^{-2}$-10^{-4} mbar). CH_5^+, $C_2H_3^+$, CH_3^+ and $C_2H_5^+$ are the dominant light hydrocarbon ions in the altitude range of 360-430 km, corresponding to pressures of $\sim 10^{-3}$-2×10^{-4} mbar. CH_5^+ is destroyed by dissociative recombination while CH_3^+ reacts with H_2 to produce CH_5^+ or undergoes dissociative recombination, at 400 km (7×10^{-4} mbar). C_2H_x ions are produced at 350-420 km altitude (3×10^{-3}-4×10^{-4} mbar), where reactions with methane ($CH_3^+ + CH_4 \rightarrow C_2H_5^+ + H_2$) and acetylene ($CH_5^+ + C_2H_2 \rightarrow C_2H_3^+ + CH_4$) were found to be the dominant ones above 350 km (3×10^{-3} mbar). Below 350 km, the dominant pathway to C_2H_x ions production becomes photoionization of C_2H_2, C_2H_4, and C_2H_6. Near 320 km (7×10^{-3} mbar), C_2H_x ions are found to be efficiently converted into C_3H_x and C_4H_x ions through reactions with neutral hydrocarbons. Among these, reactions involving C_2H_x ions (x= 2-6) with unsaturated hydrocarbons such as C_2H_2 were found to be more efficient that those with saturated hydrocarbons such as methane and ethane. The larger hydrocarbon ions are then lost through dissociative recombination around 320 km.

Kim and Fox (1994) note that carbon-adding reactions may continue until the carbon-growing hydrocarbon ion recombines, leading to the production of larger neutral hydrocarbons, some of which could condense to form hazes due to their low saturation vapor pressure. However, detailed calculations of the heavier hydrocarbon production rate require a large chemical network.

Perry et al. (1999) expanded on this approach and added the effect of precipitating auroral electrons on the hydrocarbon ion chemistry. They calculated the density profile for 21 ions and neutral species, and the electronic transport was performed using a multistream electron-transport code. Mono-energetic electron beams were assumed with energies ranging from 20-100 keV with their energy flux calibrated to produce 60 kR of H_2 Lyman-band emission, in agreement with HST observations of Kim et al. (1997). The mixing ratio of stable hydrocarbons such as CH_4, C_2H_4, and C_2H_6 were held constant below the 4-5 μbar level, based on Voyager stellar occultation measurements as well as photochemical calculations from Gladstone et al. (1996). In order to account for the location of the methane homopause at higher altitude in the auroral regions, they tested three model atmospheres, with homopause altitudes ranging from 375 to 505 km.

Ion production peaks near the electron energy deposition peak, located around 300 km, and depends significantly on both the assumed homopause altitude and precipitating electron energy. Perry et al. (1999) found that the major ions produced are transformed by ion-molecule reactions, with production through direct electron impact playing a smaller role. About 50 km below the H_3^+ density peak, i.e., 400-475 km depending on the model parameters, lies the CH_5^+ density peak, produced from the reaction between CH_4^+ and H_2. In between both density peaks lies the CH_3^+ density peak, though predicted to be two orders of magnitude smaller than that of CH_5^+. Overall, the ion density profiles were similar to those calculated by Kim and Fox (1994), but with abundance peaks one order of magnitude greater in the auroral region.

Combining the extended neutral chemical network from Gladstone et al. (1996) with the ion-neutral chemical reactions from Perry et al. (1999), Wong et al. (2000) developed a model to quantitatively assess the formation of benzene (C_6H_6) and polycyclic aromatic hydrocarbons (PAH). They included nearly a hundred reactions to simulate the formation of PAHs, up to pyrene ($C_{16}H_{10}$), using a chemical scheme proposed in flame chemistry experiments, where the abundance of PAHs and efficiency of soot formation can be explained under the H-abstraction-C_2H_2 mechanism (e.g. Wang and Frenklach 1994). They predicted the peak abundance of several PAHs to be located in the 0.1-0.01 mbar, and demonstrated that, by turning off the ion-neutral reactions, the predicted benzene concentration was decreased by a factor of 550.

Chemical calculations demonstrate that the production of benzene and aromatic ring species are increased in Jupiter's high-latitude auroral environment. The microphysical processes from which these aromatic species subsequently form aerosols was studied by Friedson et al. (2002). Using the model output from Wong et al. (2000), Friedson et al. (2002) implemented an aerosol formation microphysical model that controls their nucleation, growth, and sedimentation, based on numerical tools developed by Toon et al. (1988). Using the PAH naming convention from Wang and Frenklach (1994), where A_i represents an aromatic molecule of i fused rings (e.g., A_1, A_2, and A_4 are respectively benzene, naphthalene, and pyrene), they estimated that homogeneous nucleation of the larger PAHs considered (A_4) become important near 0.2 mbar through Brownian coagulation due to their high saturation ratios. The authors however noted the lack of experimental data to compute the homogeneous nucleation rate of A_3 and A_4 PAHs. These are important because they then serve as condensation nuclei through the more efficient heterogeneous nucleation for the lighter PAHs as they sediment down into the lower stratosphere.

The vertical distribution of the produced aerosols as a function of their size then results from an interplay between the sedimentation and the coagulation removal timescales. Above the 1-mbar pressure level, the sedimentation time of small particles is short compared to their coagulation one. Below the 1-mbar pressure level, the coagulation timescale becomes shorter than the sedimentation time and particles coagulate into larger ones. Friedson et al. (2002) noted the importance of the fractal nature of the particles, as the fall time of fractal aggregates is longer than for spherical particles. This leads to the production of larger particles at a given pressure level in the case of fractal aggregates. At 20 mbar and using two extreme fractal natures of the produced aerosols (spherical and of fractal dimension of 2.1), they predicted the mean particle radius to be between 0.1-0.7 μm.

An indirect proof of the aerosol growth with depth in Jupiter's auroral regions was suggested by Cavalié et al. (2023b) to explain the HCN depletion observed at polar latitudes and pressure levels $>$ 0.1 mbar (Fig. 8). They hypothesized that HCN bonded onto the mid-sized aerosols modeled by Friedson et al. (2002). Laboratory work led by Perrin et al. (2021) under Titan conditions in terms of composition (95% N_2 - 5% CH_4 mixture) demonstrated

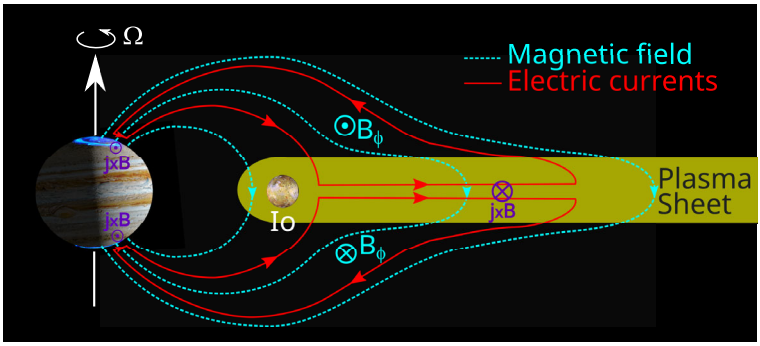

Fig. 11 Magnetosphere-ionosphere coupling at Jupiter following the corotation-enforcement theory. Adapted from Cowley and Bunce (2001) and Bonfond et al. (2020). Field-line currents develop in the middle-magnetosphere (20-60 R_J) in response of the magnetodisk plasma lagging behind corotation, resulting in an exchange of momentum with the Jovian ionosphere

that ionizing radiation first leads to the formation of small aerosols. These eventually bond with HCN as soon as they reach the size modeled by Friedson et al. (2002) in the 0.1-1 mbar region.

The observed distribution of polar aerosols, combined with the observed depletion of HCN, suggests that they are both affected by the polar atmospheric dynamics. We now briefly discuss observational constraints of the upper atmosphere dynamics.

4 Magnetosphere-Ionosphere Coupling: Consequence for Stratospheric Dynamics

Jupiter's volcanically-active moon Io is the major source of plasma within the Jovian magnetosphere. Over a ton per second of sulfur dioxide escapes from the moon as a neutral cloud around the moon. High-energy electrons trapped in Jupiter's magnetosphere dissociate and ionize the neutral material, producing ions which get picked up by Jupiter's strong rotating magnetic field, forming the Io plasma torus (Thomas et al. 2004; Bagenal and Dols 2020).

The plasma originating from Io expands to the outer magnetosphere and its azimuthal speed is expected to decrease with radial distance, based on the conservation of momentum. As it happens, there is a differential velocity between the flux tube, magnetically connected to the magnetospheric plasma, and the upper atmosphere of Jupiter, which exchange angular momentum through the $\mathbf{j} \times \mathbf{B}$ force (Fig. 11). This results in spinning up the magnetospheric plasma closer to co-rotation with the planetary interior, and slowing down the Jovian ionosphere below the planetary rotation rate (Hill 1979, 2001; Cowley and Bunce 2001).

Magnetosphere-ionosphere-thermosphere (MIT) models have previously been developed to investigate how such coupling affects the Jovian upper atmospheric thermal structure and dynamics (e.g. Achilleos et al. 1998; Bougher et al. 2005; Smith and Aylward 2009; Tao et al. 2009; Yates et al. 2012; Ray et al. 2015). Since the focus of this paper is on the stratospheric chemical distributions, more extensive discussion on this topic is deferred to a previous review paper (e.g. Bougher et al. 2008). However, we highlight the observational proofs of this momentum exchange.

In what follows, we use the term ion and neutral winds for winds measured on ion species (H_3^+) and neutral species (H_2, HCN, CO, etc.). The first evidence of the ionosphere circulation was observed in H_3^+ using CSHELL, a near-IR echelle spectrograph mounted at the

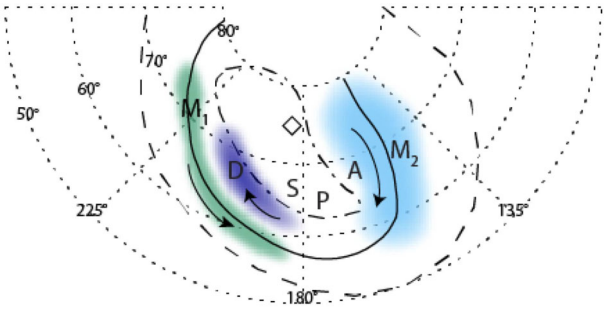

Fig. 12 Ionospheric flow measured around the Jovian north pole and shown as a north polar projection. The M_2 and D ionospheric winds are counter-rotating, while M_1 is super-rotating. The solid black line represents the position of the peak H_3^+ intensity. The diamond represents the center position of the aurora, as defined by Grodent et al. (2003), the dashed line represents the Io footprint location from model of Grodent et al. (2008). The dot-dash line marks the location of the fixed dark polar region, as defined by Stallard et al. (2003). Figure from Johnson (2018)

IRTF (Rego et al. 1999). They measured the Doppler shift of the 3.953 μm H_3^+ emission line in the auroral region induced by supersonic winds in Jupiter upper stratosphere. They found counter-rotating winds, i.e., flowing opposite to the planetary rotation, in both hemispheres. From an observer's point of view, this corresponds to a clockwise wind around the polar region. Ion winds were found near Jupiter's main auroral oval, with velocities of 2.7±0.3 and 2.9±0.3 km/s in the northern and southern hemispheres, respectively.

This work was extended by Stallard et al. (2001, 2003), using additional CSHELL observations of the same spectral line. They found velocities of the electrojet around the main oval in the 0.5-1.5 km/s range, as measured from positioning the slit over several cross-section across the auroral region. Stallard et al. (2003) transformed these velocities into a reference frame where the rotation of the magnetic pole was set to zero, and identified a region located within the polar aurora that was close to stationary, which was termed the fixed dark polar region. Near-stagnation in the ionosphere in the rest frame of the magnetic pole suggests a coupling to the solar wind. However, it is unknown whether the coupling is through a Dungey-like single-cell open field and return flow (Cowley et al. 2003) or Kelvin-Helmholtz instabilities in viscous flow interactions on the dawn flank (Delamere and Bagenal 2010).

Chaufray et al. (2011) used observations made with the Fourier Transform Spectrometer instrument at the Canada-France-Hawaii-Telescope to measure the thermospheric wind velocities on two different species; H_2 and H_3^+. They used the H_2 $S_1(1)$ quadrupole line at 2.122 μm (4712.9 cm^{-1}), and the H_3^+ 2 ν_2 R(7,7) line at 2.113 μm (4732.5 cm^{-1}) to derive the velocities from both ion and neutral species in the northern auroral region. The measured wind field in the auroral region was ∼3.1 ±0.4 km/s for the ion wind from H_3^+ and they derived an upper limit for the neutral wind velocity of 1 km/s from H_2.

Additional observations of the 3.953 μm H_3^+ line were subsequently recorded using the Cryogenic Infrared Echelle Spectrograph (CRIRES) instrument at the European Southern Observatory Very Large Telescope (VLT). Johnson et al. (2017) derived the ion wind field in the northern auroral region at higher spatial resolution. Similar to Rego et al. (1999) and Stallard et al. (2001) they found a counter-rotating wind located near the main oval flowing at around 1.5 km/s on the dusk side of the main oval, and 2.2 km/s in a region poleward of the main oval on the dawn side (see Fig. 12). Errors on the measured winds were estimated to be ± 0.3 km/s. Johnson et al. (2017) measured super-rotating winds flowing equatorward

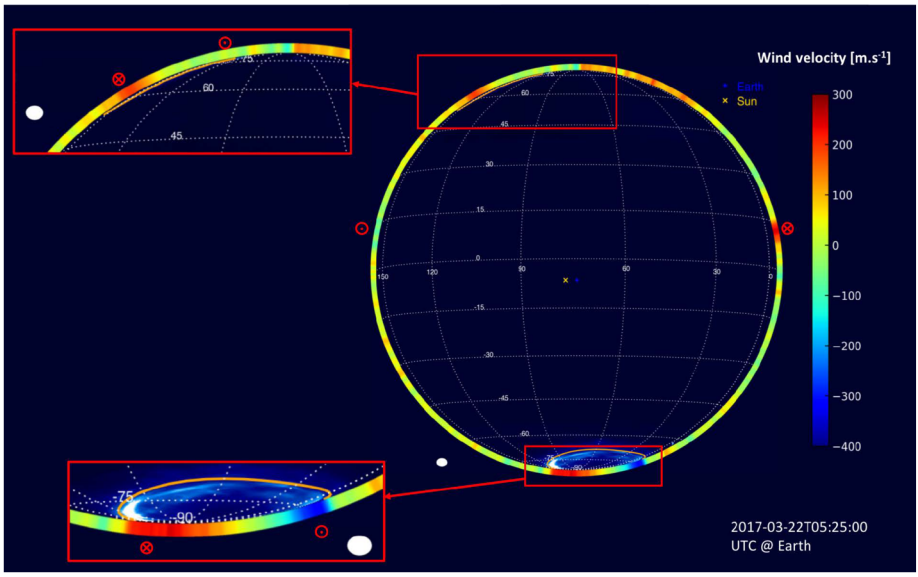

Fig. 13 Jupiter's UV aurora and stratospheric winds. This composite image shows the line-of-sight (LOS) wind velocities (in $\mathrm{m\,s^{-1}}$) derived from the ALMA observations and the statistical emission of the aurorae (Clarke et al. 2009) in the configuration of the ALMA observations. The northern and southern aurora regions are best seen in the dedicated zoomed-in quadrants. The M = 30 footprints of the magnetic field model from Connerney et al. (2018) are good markers of the positions of the main ovals as seen by Juno-UVS (Gladstone et al. 2017) and are plotted in orange. The white ellipses indicate the spatial resolution of the ALMA observations. The directions of the strongest winds in the equatorial and auroral regions are indicated with the red ⊙ and ⊗ symbols. Image reproduced from Cavalié et al. (2021), copyright by the author(s)

of the main oval with velocities of $\sim$ 0.7 km/s, also previously identified by Rego et al. (1999) and Stallard et al. (2001).

Wang et al. (2023) recently observed the quadrupole H_2 line, as well as the overtone H_3^+ lines using the Keck II/NIRSpec instrument, allowing the simultaneous derivation of the ion and neutral winds for the first time. The measured ion wind field is consistent with the past H_3^+ monitoring campaigns of Stallard et al. (2003) and Johnson et al. (2017), with globally counter-rotating jets on the dusk sector and in the dawn polar region. By subtracting the neutral winds measured on H_2 from the ionospheric winds measured in H_3^+, Wang et al. (2023) derived the effective ion winds for the first time, providing critical constraints on how the ion winds progressively drag the neutral atmosphere with increasing pressure.

One last piece of the puzzle was brought by Cavalié et al. (2021), who targeted several post SL9-species (HCN and CO) using ALMA. Figure 13 shows the measured wind-induced Doppler shift measured on the HCN (4-3) line at 354.505 GHz. This dataset provides neutral wind information for the first time in Jupiter's stratosphere at a pressure level of 0.1 mbar at high latitudes, and around 3 mbar at lower latitudes.

Cavalié et al. (2021) measured counter-rotating neutral winds flowing in the southern polar region, with velocities of 350 $\pm$ 20 m/s around the dusk side of the main oval (eastern limb) and 200 $\pm$ 20 m/s around the dawn side of the main oval (western limb). They also detected hints of the northern hemisphere wind pattern counterpart, but because the observation geometry of the northern polar region was not favorable at that time, additional

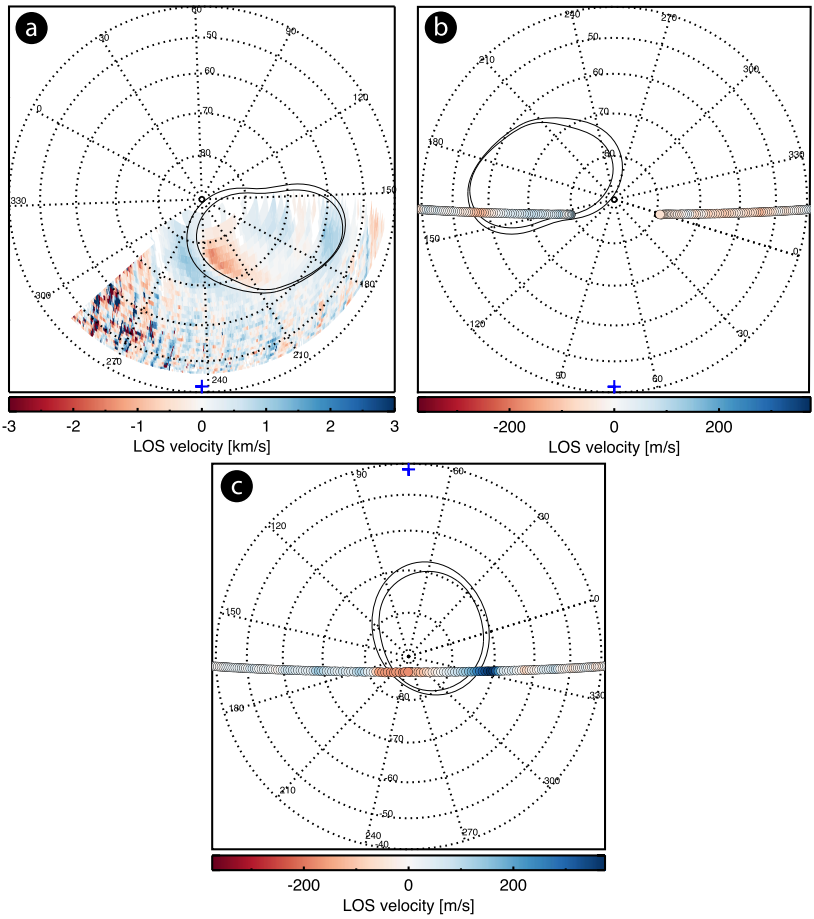

Fig. 14 Panel a: northern electrojet wind measurements on H_3^+ recorded at CML of 242°W (Johnson et al. 2017). Panel b and c: neutral stratospheric wind measurements on HCN from ALMA at CML ∼73°W in the northern and southern hemisphere, respectively (Cavalié et al. 2021). The observation central meridian longitudes are indicated as blue crosses. All winds are expressed in a reference frame that is rotating with the planet

measurements of the northern polar region are needed to fully characterize the neutral wind regime in that hemisphere.

Figure 14 compares the ionospheric wind derived from H_3^+ observations performed with VLT/CRIRES on 31 December 2012 (upper left panel) with the stratospheric neutral wind derived from HCN observations performed by ALMA on 22 March 2017 (upper right and bottom panels). The northern ionospheric and stratospheric winds were recorded at Central Meridian Longitudes (CML) almost half a Jupiter rotation apart (CML of 242°W and 73°W, respectively), though in different years. These observations suggest that the equatormost part of the electrojet (Fig. 14a at longitudes 150°W-180°W and latitudes 55°N-60°N) might be stable over time and potentially extends down to the neutral atmosphere at least to sub-mbar levels (Fig. 14b at longitudes 150°-165° and latitude 55°N-60°N), although the detailed mechanism needs to be worked out. This conclusion can also be derived from

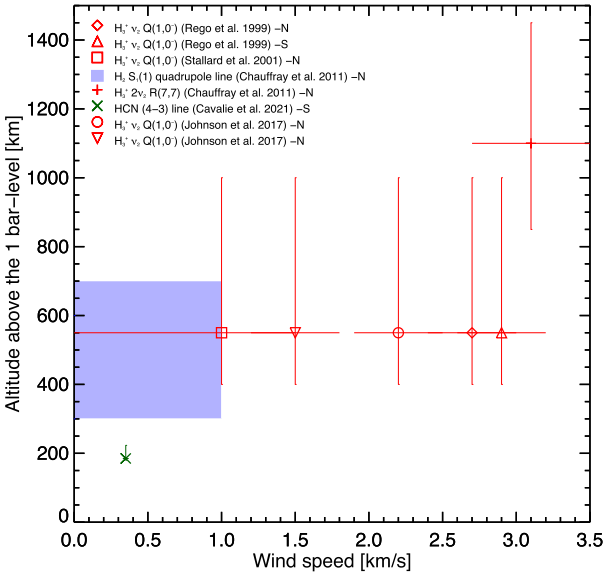

Fig. 15 Summary of the ionospheric and stratospheric wind measurements in Jupiter's stratosphere. The label describes the spectral information of the line, as well as the hemisphere (N/S) targeted. Information about the altitude sensitivity of these measurements are derived from Melin et al. (2005) and Grodent et al. (2001). Wind measurements from Chaufray et al. (2011) and derived from the H_2 $S_1(1)$ quadrupole line provided an upper limit of 1 km/s, over the altitude range of 300–700 km (see text for details)

observations of Chaufray et al. (2011) and Wang et al. (2023) indicating the co-location of ion and neutral winds, though derived from slightly different altitudes. The southern polar region stratospheric winds are more obvious, though additional VLT/CRIRES observations of the southern hemisphere would be needed to reinforce this conclusion.

The neutral wind measurements derived from HCN and H_2 across the polar stratosphere do not indicate super-corotating flows, while the ion wind measurements consistently do (Rego et al. 1999; Stallard et al. 2001; Johnson et al. 2017; Wang et al. 2023). Morphology of the sub-rotating neutral winds from Wang et al. (2023) match fairly well the ion winds one measured on the same dataset, without the super-rotating ion winds. Models of this interaction suggest the neutral atmosphere is slow to react to changing ion winds with ion drag. Notably, Tao et al. (2009) showed that acceleration of the neutral atmosphere caused by ion drag decreases with increasing altitude. Using calculations from Tao et al. (2009), Wang et al. (2023) estimated that this process takes about 10 Jovian days to accelerate the neutral atmosphere to ∼1 km/s at an altitude of 1000 km, while it takes about 70 Jovian days to do so at 400 km altitude. As a result, while H_3^+ takes on any asymmetric flows in the magnetosphere, e.g. from super-rotation as measured on the dayside magnetosphere (Krupp et al. 2001) and modeled (Chané et al. 2013), the neutral atmosphere probably does not.

Figure 15 summarizes the aforementioned ionospheric and stratospheric neutral wind measurements. The altitude region at which the H_3^+ observations are sensitive to are taken from Melin et al. (2005), which uses the atmospheric model of Grodent et al. (2001). The altitude range of these H_3^+ observations are estimated from the FWHM of the line emission intensity. For instance, the altitude sensitivity of the fundamental ν_2 $Q(1,0^-)$ line is 550^{+450}_{-150} km (∼ 4×10^{-4}-4×10^{-6} mbar). We assumed the altitude at which the $2\nu_2$ R(7,7) line senses to be 1100^{+350}_{-250} km (∼ 1×10^{-5}-3×10^{-7} mbar), based on the altitude sensitivity range of the $2\nu_2$ lines calculated by Melin et al. (2005). The pressure range at which the HCN (4-3) line forms is $0.08^{+0.02}_{-0.06}$ mbar, assuming the peak and the FWHM of the line forming contribution function from Cavalié et al. (2021). This corresponds to an altitude range of 185^{+38}_{-5} km, using the Grodent et al. (2001) model. The altitude sensitivity range of the H_2 $S_1(1)$ quadrupole line was calculated to be 300-700 km, based on Chaufray et al. (2011)

and Bougher et al. (2005). Note that additional models of Tao et al. (2011) predict sensibly similar peak UV (H_2) and IR (H_3^+) emission altitudes.

5 Summary and Outstanding Questions

Observations of the Jovian upper atmosphere in the UV, IR and mm/sub-mm all provide evidence that the chemical distributions and thermal structure are broadly influenced by auroral particle precipitation.

Mid-IR observations of the chemical distributions suggest that several light hydrocarbons (C_2H_2, C_2H_4, C_2H_6) are locally affected near the statistical location of the main auroral region. The derived C_2H_2 and C_2H_4 abundances are enhanced at the mbar and sub-mbar levels consistently in all mid-IR datasets. The situation for C_2H_6 is interesting as earlier space-based observations suggested it was depleted within the auroral oval at 5 mbar, but enhanced at the same latitude away from the oval, implying some chemical conversion, as the total C_2H_x content seems to be zonally conserved at the mbar level (Sinclair et al. 2017). Recent datasets recorded at high spatial resolution confirm that C_2H_6 is enhanced at high latitudes (Sinclair et al. 2023; Rodríguez-Ovalle et al. 2024), and likely affected by modulation in the magnetospheric activity, possibly linked with changes in the solar wind conditions (Sinclair et al. 2023).

Ultraviolet observations with Juno-UVS have provided another important piece of the puzzle. Solar-reflected UV light captured by UVS around 175-190 nm carry the absorption signature of C_2H_2 and C_6H_6, probing their total column abundance down to 5-50 mbar (Giles et al. 2023). Juno-UVS observations show that C_2H_2 is enhanced up to a factor of 3.5 around the polar auroral region, compared to the non-auroral atmosphere, and possibly suggest that C_6H_6 is enhanced around the same region. Since these observations probe deeper than the mid-IR observations and reflect the total column abundance, the enhancements are more homogeneous across the polar auroral regions.

ALMA is an outstanding tool for millimeter observations of Jupiter and can provide chemical distributions (Cavalié et al. 2023b), as well as auroral (Cavalié et al. 2021) and equatorial neutral winds (Benmahi et al. 2021) in a single observation run. One of the most striking features from these datasets is the almost 2 orders of magnitude drop in the HCN column density above both poles, initially observed by Cassini-CIRS over the south pole (Lellouch et al. 2006). ALMA observations provide a detailed mapping of this depletion, and demonstrate that it is located at pressures where large auroral-produced aerosols (Friedson et al. 2002) are expected. Cavalié et al. (2023b) even suggest that HCN could have an auroral production term at higher altitude.

Neutral photochemical models of the stratosphere have attempted to reproduce the meridional trends in the C_2H_2 and C_2H_6 observed by Cassini-CIRS and retrieved by Nixon et al. (2007, 2010), which initially excluded the longitudinal range covering the auroral oval. The anti-correlated trend in both hydrocarbon abundances (C_2H_2 decreasing towards the pole, while C_2H_6 increases towards the pole) still remains unexplained. It was initially thought that, because both hydrocarbons have a different lifetime, there may be a circulation pattern that could produce such trend. Using a coupled photochemical-transport 2D-model, Hue et al. (2018) showed that both trends can not be reproduced by a combination of advective and diffusive transport, and that another chemical process must be preferentially affecting one of these hydrocarbons.

Ion-neutral chemical models provide insights on how the charged particle precipitation affect the neutral species. Kim and Fox (1994) predicted that CH_5^+, $C_2H_3^+$, CH_3^+ and $C_2H_5^+$

are the dominant hydrocarbon ions at pressures of 7×10^{-4} mbar and above in the upper atmosphere. They showed that reactions involving C_2H_x ions with unsaturated hydrocarbons such as C_2H_2 are more efficient than with saturated hydrocarbons (e.g., CH_4 and C_2H_6). These could possibly explain the trend seen by Sinclair et al. (2017) where C_2H_2 is locally enhanced around the polar auroral region, and converted into C_2H_6 away from that region, although Kim and Fox (1994) did not study how the auroral electron precipitations would affect the neutral hydrocarbon abundances. They noted that the combination of hydrocarbon ions could lead to the formation of larger neutral hydrocarbons.

The link between the formation of large hydrocarbon molecules with the observation of the polar hazes on Jupiter has been established for years (Hord et al. 1979; Pryor and Hord 1991). Work by Zhang et al. (2013) using Cassini/ISS limb-darkening observations at multiple phase angles showed the existence of two types of aerosols; one consisting of compact sub-micron particles, and the other consisting of fractal aggregates composed of small monomers. The high-latitude regions were best reproduced assuming fractal aggregated particles consisting in thousands of ~10 nm monomers, with column densities ~2 orders of magnitude greater than around the low-latitude regions. Wong et al. (2000, 2003) and Friedson et al. (2002) estimated the amount of large hydrocarbons produced from ion-neutral reactions, and developed a microphysical model of the auroral haze formation. Hydrocarbons are produced from methane chemistry and ion-neutral chemistry around the nbar level, they are predicted to grow into larger hydrocarbon fused rings around 10 nbar. They may subsequently nucleate through homogeneous nucleation at the submbar level, and grow through heterogeneous nucleation while sedimenting. At the mbar level, they coagulate and condensate into sub-microns aerosols.

One important piece from two decades of H_3^+ observations as well as ALMA observation concerns the dynamical coupling of the upper atmosphere with the magnetosphere, potentially affecting the chemical spatial distribution. H_3^+ observations provided evidence of an ionospheric auroral electrojet (Rego et al. 1999; Stallard et al. 2001; Johnson et al. 2017; Wang et al. 2023) flowing near the main oval opposite to the planetary rotation, and may extend to the neutral atmosphere down to the sub-mbar level, i.e., several hundred km below the electrojets.

These electrojets corotate with Jupiter at a rate of 10 hours, while the tropospheric weather layer does not rotate exactly at that rate. There is a progressive dynamical decoupling operating between (i) the ionospheric vortex flowing along the main oval, and (ii) the background neutral atmosphere underneath. Depending on the pressure level probed, different trends are expected for the chemical distributions. At the nbar to mbar levels, aurorally-produced species may be confined within the main oval as a result of short chemical lifetimes possibly combined with the dynamical confinement caused by the electrojet. This seems to be what the hydrocarbon distributions sensed by mid-IR observations are suggesting (e.g. Sinclair et al. 2018, 2023). At the 10-100 mbar level, the situation is opposite and the chemical distributions are longitudinally homogeneous, as seen, e.g., in the polar haze distributions (Zhang et al. 2013; Rogers et al. 2022; Hueso et al. 2023), also shown on Fig. 6. In between these two pressure levels, chemical distributions are expected to display a mixture of both morphologies. This may be the case for the Juno-UVS reflected sunlight observations in the southern hemisphere (Fig. 3), which shows a C_2H_2 enhancement within the main oval, superposed with a longitudinally-homogeneous background enhancement that mimics the polar haze distributions (Giles et al. 2021a).

Figure 16 summarizes the various processes discussed in this paper. Note that, although ALMA data have unequivocally indicated the existence of stratospheric neutral winds co-located with the position of the southern main auroral emission (Cavalié et al. 2021), it

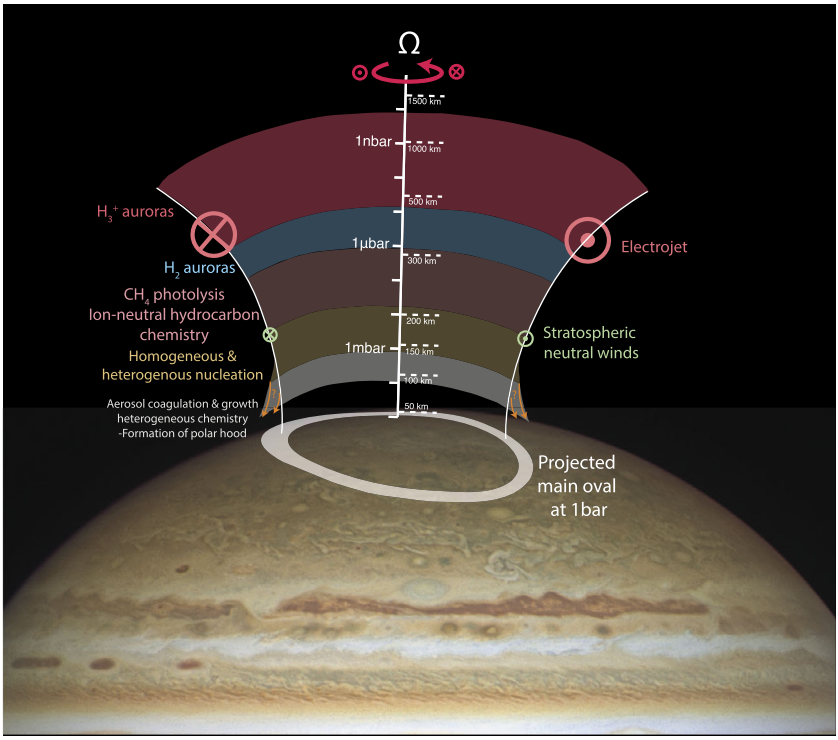

Fig. 16 Summary schematics of selected chemical distributions across Jupiter's polar region. Particle precipitation leads to the formation of H_3^+ in the ionosphere, and to UV-auroras through the H and H_2 emissions at the μbar level. Around the μbar level and below, solar-UV photolysis as well as charged particle precipitations leads to the formation of hydrocarbons. As hydrocarbons diffuse downward, they combine into heavier hydrocarbons to form aerosols. HCN produced in the upper atmosphere, possibly from N_2 destruction, get incorporated into aerosols before they reach ~2 mbar or below. Background image credits: NASA, ESA, A. Simon, M. H. Wong, and J. DePasquale

only provided hints of that circulation in the northern hemisphere due to the observational geometry. Some of the remaining outstanding questions that need to be answered include:

- What are the exact chemical pathways producing the enhanced hydrocarbons in the polar region, given the constraints brought by the Juno in-situ particle measurements across the polar regions?
- Do Jupiter's UV auroral emissions affect the high-latitude hydrocarbon distributions through photolysis?
- What is the origin of the double temperature peak seen in the mid-IR observations, i.e., around the 1 mbar and 10 μbar levels?
- What are the physical mechanisms causing the higher methane homopause in the polar auroral region?
- Where does the decoupling between the electrojet and the lower stratosphere occur? How does this decoupling affect the chemical distributions?
- Given the larger tilt in the northern magnetic dipole compared to the southern one, how different is the decoupling of the electrojet and the background neutral atmosphere between both hemispheres? In other words, is the southern auroral circulation more efficient at dynamically confining the aurorally-produced species and hazes?

• Does the super-rotating electrojet found equatorward of the northern main oval propagate down to the stratosphere?

• What is the pattern of the residual circulation in the polar region, and how does it affect the distribution of chemical species?

• How do the polar aerosols produce the complex pattern of wavy structures at different latitudes?

• How often auroral events form specific patches of aerosols or concentrated chemicals associated to polar dark patches as seen in the UV (Porco et al. 2003; Tsubota et al. 2024)? Are these patches set in motions by the same wind propagating from the ionosphere to the bottom of the stratosphere?

To answer some of these questions, continuing the monitoring in the near- and mid-IR, as well as well in the millimeter range is crucial. For instance, ALMA alone can provide the distributions of several key chemical species as well as the winds with a single dataset of moderate exposure time (<1 hr on-source, thus enabling longitudinal coverage with limited longitudinal smearing) (Cavalié et al. 2021). Modeling effort should be pursued in accounting for the ion-neutral chemical network available in the literature in Jovian conditions (Loison et al. 2015; Dobrijevic et al. 2016; Wong et al. 2000; Brown et al. 2024), while including the knowledge of the charged particle precipitating energy flux measured by Juno. Some of the main ions predicted are CH_5^+, $C_2H_3^+$, CH_3^+ and $C_2H_5^+$ (Kim and Fox 1994), and attempting to detect them will help to constrain ion-neutral photochemical models. Laboratory work is required to identify the spectral signatures of these ions and enable their detection with observatories such as JWST.

Finally, the JUICE mission will undoubtedly help to improve our understanding of the chemistry and dynamics of Jupiter's polar regions with its 3-year Jupiter tour including equatorial and inclined orbits. JUICE's comprehensive payload includes remote sensing instruments, spanning from the UV to the sub-mm, as well as in situ experiments (Fletcher et al. 2023).

Appendix A: Coverage of Mid-IR and UV Observing Campaigns

Figures 17, 18, 19, and 20 represent the spatial coverage of the mid-IR and UV observations campaign from which the polar stratospheric hydrocarbon trends (Tables 1, 2, 3, and 4) were derived.

Note that the vertical sensitivity of the mid-IR observations depends on the spectral setting as well as the vertical temperature profile. Observations at higher resolving power are generally sensitive to a greater pressure range. Upper-stratospheric heating, e.g. near the polar hot spot, also causes secondary sensitivity peaks in the contribution functions at higher altitudes (e.g. Sinclair et al. 2019). Although Figs. 17, 18, 19, and 20 show the pressure range over which these observations are sensitive to, the corresponding tables only provide the trends at the pressure level at the respective contribution functions peak.

The reflected sunlight observation from Juno-UVS are sensitive to the total column abundance down to the 5-50 mbar (Melin et al. 2020; Giles et al. 2021a, 2023).

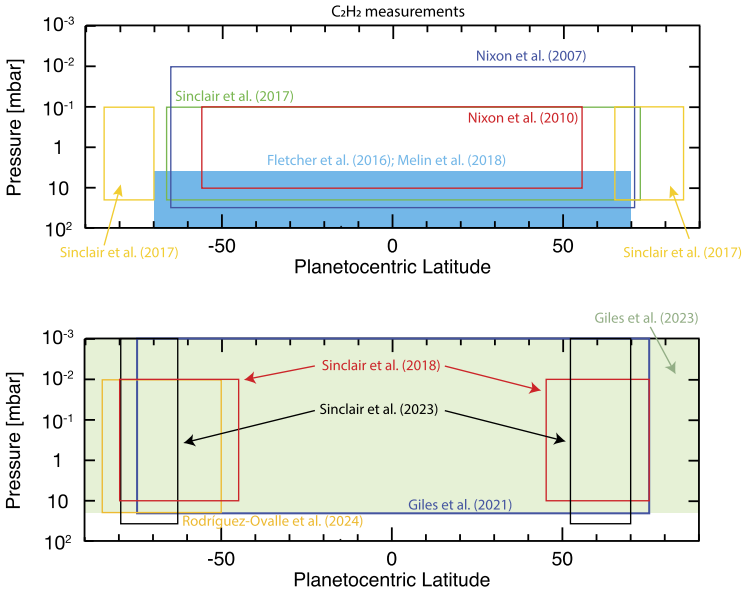

Fig. 17 Spatial coverage and vertical sensitivity of the mid-IR and UV observing campaigns that derived spatial distribution of acetylene (C_2H_2), from Table 1. The coverage from these measurements were broken into two plots for clarity

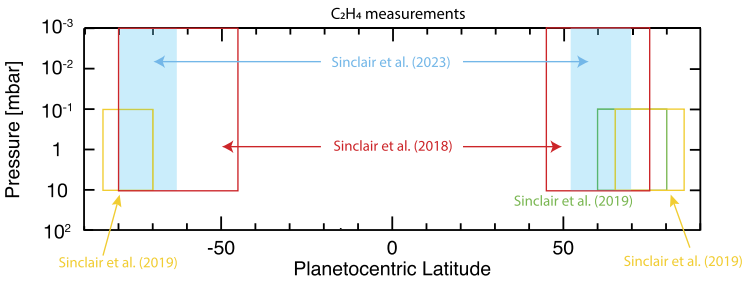

Fig. 18 Spatial coverage and vertical sensitivity of the mid-IR observing campaigns that derived spatial distribution of ethylene (C_2H_4), from Table 2

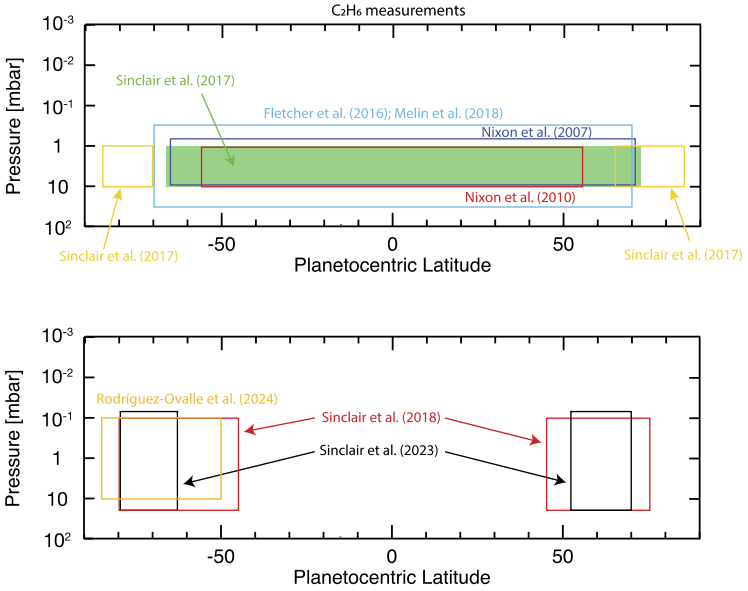

Fig. 19 Spatial coverage and vertical sensitivity of the mid-IR observing campaigns that derived spatial distribution of ethane (C_2H_6), from Table 3. The coverage from these measurements were broken into two plots for clarity

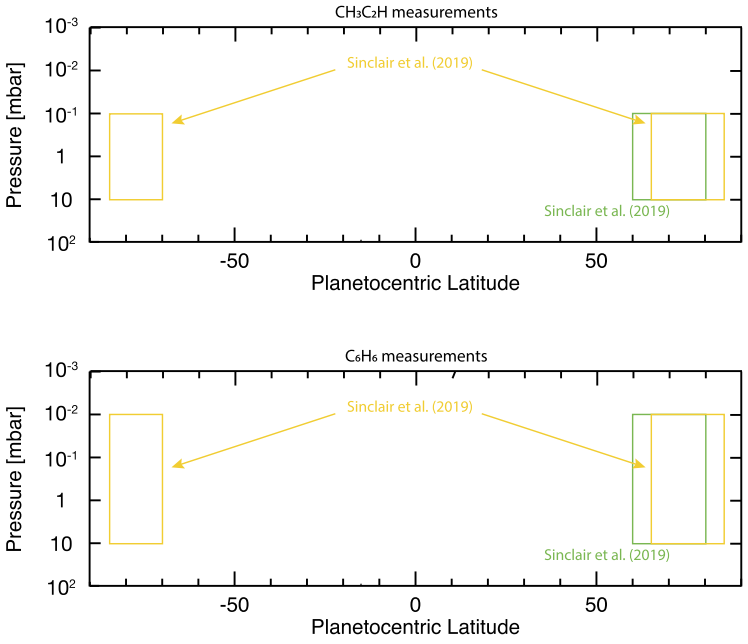

Fig. 20 Spatial coverage and vertical sensitivity of the mid-IR observing campaigns that derived spatial distribution of methylacetylene (CH_3C_2H, top panel) and benzene (C_6H_6, bottom panel), from Table 4. Note that JWST/MIRI provided information about the benzene distribution across the southern polar stratosphere of Jupiter (Rodriguez-Ovalle et al. 2023), but the authors concluded that these measurements were not particularly sensitive to the benzene vertical distribution

Acknowledgements We thank Bertrand Bonfond for providing Fig. 11.

Funding V. Hue acknowledges support from the French government under the France 2030 investment plan, as part of the Initiative d'Excellence d'Aix-Marseille Université – A*MIDEX AMX-22-CPJ-04. French authors acknowledge the support of CNES to the Juno mission. A subset of the work presented in this paper was carried out at the Jet Propulsion Laboratory, California Institute of Technology, under a contract with the National Aeronautics and Space Administration (NASA). The material is based upon work supported by the NASA under Grant NNH20ZDA001N issued through the Solar System Observations Planetary Astronomy program. R. Hueso was supported by grant PID 2019-109467GB-I00 funded by MCIN/AEI/10.13039/501100011033/ and was also supported by Grupos Gobierno Vasco IT1742-22. The support of T. K. Greathouse and R. S. Giles was funded by the NASA's New Frontiers Program for Juno via contract NNM06AA75C with the Southwest Research Institute. R. E. Johnson is supported by NERC grant NE/W002914/1. C. A. Nixon was supported for his work on this paper by NASA GSFC SSED Strategic Science funding.

Declarations

Competing Interests The authors declare that they have no conflicts of interest.

References

Achilleos N, Miller S, Tennyson J, et al (1998) JIM: a time-dependent, three-dimensional model of Jupiter's thermosphere and ionosphere. J Geophys Res 103(E9):20089–20112. https://doi.org/10.1029/98JE00947

Allen M, Yung YL, Waters JW (1981) Vertical transport and photochemistry in the terrestrial mesosphere and lower thermosphere (50-120 km). J Geophys Res 86:3617–3627. https://doi.org/10.1029/JA086iA05p03617

Badman SV, Branduardi-Raymont G, Galand M, et al (2015) Auroral processes at the giant planets: energy deposition, emission mechanisms, morphology and spectra. Space Sci Rev 187(1–4):99–179. https://doi.org/10.1007/s11214-014-0042-x

Bagenal F, Dols V (2020) The space environment of Io and Europa. J Geophys Res Space Phys 125(5):e27485. https://doi.org/10.1029/2019JA027485

Banfield D, Gierasch PJ, Squyres SW, et al (1996) 2 μm spectrophotometry of Jovian stratospheric aerosols – scattering opacities, vertical distributions, and wind speeds. Icarus 121:389–410. https://doi.org/10.1006/icar.1996.0095

Banfield D, Conrath BJ, Gierasch PJ, et al (1998) Near-IR spectrophotometry of Jovian aerosols – meridional and vertical distributions. Icarus 134(1):11–23. https://doi.org/10.1006/icar.1998.5942

Barbara JM, West RA, Del Genio AD, et al (2024) A study of Jupiter's UV Great Dark Spot and tropopause to stratosphere winds in the high northern latitudes as seen by Cassini imaging. Icarus 410:115913. https://doi.org/10.1016/j.icarus.2023.115913

Barrado-Izagirre N, Sánchez-Lavega A, Pérez-Hoyos S, et al (2008) Jupiter's polar clouds and waves from Cassini and HST images 1993 2006. Icarus 194(1):173–185. https://doi.org/10.1016/j.icarus.2007.08.025

Benmahi B, Cavalié T, Dobrijevic M, et al (2020) Monitoring of the evolution of H_2O vapor in the stratosphere of Jupiter over an 18-yr period with the Odin space telescope. Astron Astrophys 641:A140. https://doi.org/10.1051/0004-6361/202038188. arXiv:2007.05415 [astro-ph.EP]

Benmahi B, Cavalié T, Greathouse TK, et al (2021) Mapping the zonal winds of Jupiter's stratospheric equatorial oscillation. Astron Astrophys 652:A125. https://doi.org/10.1051/0004-6361/202141523. arXiv:2107.06122 [astro-ph.EP]

Benmahi B, Cavalié T, Fouchet T, et al (2022) First absolute wind measurements in Saturn's stratosphere from ALMA observations. Astron Astrophys 666:A117. https://doi.org/10.1051/0004-6361/202244200

Bergin EA, Lellouch E, Harwit M, et al (2000) Submillimeter wave astronomy satellite observations of Jupiter and Saturn: detection of 557 GHZ water emission from the upper atmosphere. Astrophys J 539(2):L147–L150. https://doi.org/10.1086/312846

Bézard B, Griffith C, Lacy J, et al (1995) Non-detection of hydrogen cyanide on Jupiter. Icarus 118(2):384–391. https://doi.org/10.1006/icar.1995.1198

Bézard B, Lellouch E, Strobel D, et al (2002) Carbon monoxide on Jupiter: evidence for both internal and external sources. Icarus 159:95–111. https://doi.org/10.1006/icar.2002.6917

Bjoraker GL, Stolovy SR, Herter TL, et al (1996) Detection of water after the collision of fragments G and K of comet Shoemaker-Levy 9 with Jupiter. Icarus 121(2):411–421. https://doi.org/10.1006/icar.1996.0096

Bolton SJ, Adriani A, Adumitroaie V, et al (2017) Jupiter's interior and deep atmosphere: the initial pole-to-pole passes with the Juno spacecraft. Science 356:821–825. https://doi.org/10.1126/science.aal2108

Bonfond B, Grodent D, Gérard JC, et al (2012) Auroral evidence of Io's control over the magnetosphere of Jupiter. Geophys Res Lett 39(1):L01105. https://doi.org/10.1029/2011GL050253

Bonfond B, Yao Z, Grodent D (2020) Six pieces of evidence against the corotation enforcement theory to explain the main aurora at Jupiter. J Geophys Res Space Phys 125:e2020JA028152. https://doi.org/10.1029/2020JA028152. arXiv:2005.05938 [physics.space-ph]

Bougher SW, Waite JH, Majeed T, et al (2005) Jupiter Thermospheric General Circulation Model (JTGCM): global structure and dynamics driven by auroral and Joule heating. J Geophys Res, Planets 110(E4):E04008. https://doi.org/10.1029/2003JE002230

Bougher SW, Blelly PL, Combi M, et al (2008) Neutral upper atmosphere and ionosphere modeling. Space Sci Rev 139(1–4):107–141. https://doi.org/10.1007/s11214-008-9401-9

Broadfoot AL, Sandel BR, Shemansky DE, et al (1981) Overview of the Voyager ultraviolet spectrometry results through Jupiter encounter. J Geophys Res 86(A10):8259–8284. https://doi.org/10.1029/JA086iA10p08259

Brown ZL, Koskinen TT, Moses JI, et al (2024) A pole-to-pole map of hydrocarbons in Saturn's upper stratosphere and mesosphere. Icarus 417:116133. https://doi.org/10.1016/j.icarus.2024.116133. arXiv:2405.01763 [astro-ph.EP]

Cadle RD (1962) The photochemistry of the upper atmosphere of Jupiter. J Atmos Sci 19:281–285. https://doi.org/10.1175/1520-0469(1962)019<0281:TPOTUA>2.0.CO;2

Caldwell J, Tokunaga AT, Gillett FC (1980) Possible infrared aurorae on Jupiter. Icarus 44(3):667–675. https://doi.org/10.1016/0019-1035(80)90135-9

Cavalié T, Billebaud F, Biver N, et al (2008) Observation of water vapor in the stratosphere of Jupiter with the Odin space telescope. Planet Space Sci 56:1573–1584. https://doi.org/10.1016/j.pss.2008.04.013

Cavalié T, Biver N, Hartogh P, et al (2012) Odin space telescope monitoring of water vapor in the stratosphere of Jupiter. Planet Space Sci 61:3–14. https://doi.org/10.1016/j.pss.2011.04.001

Cavalié T, Feuchtgruber H, Lellouch E, et al (2013) Spatial distribution of water in the stratosphere of Jupiter from Herschel HIFI and PACS observations. Astron Astrophys 553:A21. https://doi.org/10.1051/0004-6361/201220797

Cavalié T, Benmahi B, Hue V, et al (2021) First direct measurement of auroral and equatorial jets in the stratosphere of Jupiter. Astron Astrophys 647:L8. https://doi.org/10.1051/0004-6361/202140330. arXiv:2103.12208 [astro-ph.EP]

Cavalié T, Lunine J, Mousis O (2023a) A subsolar oxygen abundance or a radiative region deep in Jupiter revealed by thermochemical modelling. Nat Astron 7:678–683. https://doi.org/10.1038/s41550-023-01928-8. arXiv:2305.13949 [astro-ph.EP]

Cavalié T, Rezac L, Moreno R, et al (2023b) Evidence for auroral influence on Jupiter's nitrogen and oxygen chemistry revealed by ALMA. Nat Astron. https://doi.org/10.1038/s41550-023-02016-7

Chané E, Saur J, Poedts S (2013) Modeling Jupiter's magnetosphere: influence of the internal sources. J Geophys Res Space Phys 118(5):2157–2172. https://doi.org/10.1002/jgra.50258

Chaufray JY, Greathouse TK, Gladstone GR, et al (2011) Spectro-imaging observations of Jupiter's 2 μm auroral emission. II: thermospheric winds. Icarus 211(2):1233–1241. https://doi.org/10.1016/j.icarus.2010.11.021

Clarke JT, Nichols J, Gérard JC, et al (2009) Response of Jupiter's and Saturn's auroral activity to the solar wind. J Geophys Res Space Phys 114(A5):A05210. https://doi.org/10.1029/2008JA013694

Connerney JEP, Kotsiaros S, Oliversen RJ, et al (2018) A new model of Jupiter's magnetic field from Juno's first nine orbits. Geophys Res Lett 45:2590–2596. https://doi.org/10.1002/2018GL077312

Connerney JEP, Timmins S, Oliversen RJ, et al (2022) A new model of Jupiter's magnetic field at the completion of Juno's prime mission. J Geophys Res, Planets 127(2):e07055. https://doi.org/10.1029/2021JE007055

Conrath BJ, Gierasch PJ, Leroy SS (1990) Temperature and circulation in the stratosphere of the outer planets. Icarus 83:255–281. https://doi.org/10.1016/0019-1035(90)90068-K

Cowley SWH, Bunce EJ (2001) Origin of the main auroral oval in Jupiter's coupled magnetosphere-ionosphere system. Planet Space Sci 49(10–11):1067–1088. https://doi.org/10.1016/S0032-0633(00)00167-7

Cowley SWH, Bunce EJ, Stallard TS, et al (2003) Jupiter's polar ionospheric flows: theoretical interpretation. Geophys Res Lett 30(5):1220. https://doi.org/10.1029/2002GL016030

Davis MW, Gladstone GR, Greathouse TK, et al (2011) Radiometric performance results of the Juno ultraviolet spectrograph. In: Juno-UVS. Proc SPIE, vol 8146, 814604. https://doi.org/10.1117/12.894274

de Graauw T, Haser LN, Beintema DA, et al (1996) Observing with the ISO short-wavelength spectrometer. Astron Astrophys 315:L49–L54

Delamere PA, Bagenal F (2010) Solar wind interaction with Jupiter's magnetosphere. J Geophys Res Space Phys 115(A10):A10201. https://doi.org/10.1029/2010JA015347

Dobrijevic M, Parisot JP (1998) Effect of chemical kinetics uncertainties on hydrocarbon production in the stratosphere of Neptune. Planet Space Sci 46:491–505. https://doi.org/10.1016/S0032-0633(97)00176-1

Dobrijevic M, Ollivier JL, Billebaud F, et al (2003) Effect of chemical kinetic uncertainties on photochemical modeling results: application to Saturn's atmosphere. Astron Astrophys 398:335–344. https://doi.org/10.1051/0004-6361:20021659

Dobrijevic M, Cavalié T, Hébrard E, et al (2010) Key reactions in the photochemistry of hydrocarbons in Neptune's stratosphere. Planet Space Sci 58:1555–1566. https://doi.org/10.1016/j.pss.2010.07.024

Dobrijevic M, Cavalié T, Billebaud F (2011) A methodology to construct a reduced chemical scheme for 2D-3D photochemical models: application to Saturn. Icarus 214:275–285. https://doi.org/10.1016/j.icarus.2011.04.027

Dobrijevic M, Loison JC, Hickson KM, et al (2016) 1D-coupled photochemical model of neutrals, cations and anions in the atmosphere of Titan. Icarus 268:313–339. https://doi.org/10.1016/j.icarus.2015.12.045

Drossart P, Maillard JP, Caldwell J, et al (1989) Detection of H_3^+ on Jupiter. Nature 340:539–541. https://doi.org/10.1038/340539a0

Drossart P, Bezard B, Atreya SK, et al (1993) Thermal profiles in the auroral regions of Jupiter. J Geophys Res 98(E10):18803–18812. https://doi.org/10.1029/93JE01801

Encrenaz T, Combes M, Zeau Y (1978) The spectrum of Jupiter between 10 and 13 μ. Astron Astrophys 70:29

Encrenaz T, de Graauw T, Schaeidt S, et al (1996) First results of ISO-SWS observations of Jupiter. Astron Astrophys 315:L397–L400

Encrenaz T, Drossart P, Carlson RW, et al (1997) Detection of H_2O in the splash phase of G- and R-impacts from NIMS-Galileo. Planet Space Sci 45(10):1189–1196. https://doi.org/10.1016/S0032-0633(97)00025-1

Fegley JB, Lodders K (1994) Chemical models of the deep atmospheres of Jupiter and Saturn. Icarus 110(1):117–154. https://doi.org/10.1006/icar.1994.1111

Fegley B, Prinn RG (1988) Chemical constraints on the water and total oxygen abundances in the deep atmosphere of Jupiter. Astrophys J 324:621. https://doi.org/10.1086/165922

Festou MC, Atreya SK, Donahue TM, et al (1981) Composition and thermal profiles of the Jovian upper atmosphere determined by the Voyager ultraviolet stellar occultation experiment. J Geophys Res 86:5715–5725. https://doi.org/10.1029/JA086iA07p05715

Flasar FM, Achterberg RK, Conrath BJ, et al (2005) Temperatures, winds, and composition in the saturnian system. Science 307(5713):1247–1251. https://doi.org/10.1126/science.1105806

Fletcher LN, Orton GS, Yanamandra-Fisher P, et al (2009) Retrievals of atmospheric variables on the gas giants from ground-based mid-infrared imaging. Icarus 200(1):154–175. https://doi.org/10.1016/j.icarus.2008.11.019

Fletcher LN, Greathouse TK, Orton GS, et al (2016) Mid-infrared mapping of Jupiter's temperatures, aerosol opacity and chemical distributions with IRTF/TEXES. Icarus 278:128–161. https://doi.org/10.1016/j.icarus.2016.06.008. arXiv:1606.05498 [astro-ph.EP]

Fletcher LN, Cavalié T, Grassi D, et al (2023) Jupiter science enabled by ESA's Jupiter Icy moons Explorer. Space Sci Rev 219(7):53. https://doi.org/10.1007/s11214-023-00996-6. arXiv:2304.10229 [astro-ph.EP]

Fouchet T, Lellouch E, Bézard B, et al (2000) Jupiter's hydrocarbons observed with ISO-SWS: vertical profiles of C_2H_6 and C_2H_2, detection of CH_3C_2H. Astron Astrophys 355:L13–L17. arXiv:astro-ph/0002273

Friedson AJ, Wong AS, Yung YL (2002) Models for polar haze formation in Jupiter's stratosphere. Icarus 158:389–400. https://doi.org/10.1006/icar.2002.6885

Gierasch PJ, Magalhaes JA, Conrath BJ (1986) Zonal mean properties of Jupiter's upper troposphere from Voyager infrared observations. Icarus 67:456–483. https://doi.org/10.1016/0019-1035(86)90125-9

Giles RS, Greathouse TK, Bonfond B, et al (2020) Possible transient luminous events observed in Jupiter's upper atmosphere. J Geophys Res, Planets 125(11):e06659. https://doi.org/10.1029/2020JE006659. arXiv:2010.13740 [astro-ph.EP]

Giles RS, Greathouse TK, Hue V, et al (2021a) Meridional variations of C_2H_2 in Jupiter's stratosphere from Juno UVS observations. J Geophys Res, Planets 126(8):e06928. https://doi.org/10.1029/2021JE006928. arXiv:2107.11295 [astro-ph.EP]

Giles RS, Greathouse TK, Kammer JA, et al (2021b) Detection of a bolide in Jupiter's atmosphere with Juno UVS. Geophys Res Lett 48(5):e91797. https://doi.org/10.1029/2020GL091797. arXiv:2102.04511 [astro-ph.EP]

Giles RS, Hue V, Greathouse TK, et al (2023) Enhanced C_2H_2 absorption within Jupiter's southern auroral oval from Juno UVS observations. J Geophys Res, Planets 128(2):e2022JE007610. https://doi.org/10.1029/2022JE007610. arXiv:2302.10946 [astro-ph.EP]

Gillett FC, Low FJ, Stein WA (1969) The 2.8-14-MICRON spectrum of Jupiter. Astrophys J 157:925. https://doi.org/10.1086/150124

Gladstone GR, Allen M, Yung YL (1996) Hydrocarbon photochemistry in the upper atmosphere of Jupiter. Icarus 119(1):1–52. https://doi.org/10.1006/icar.1996.0001

Gladstone GR, Persyn SC, Eterno JS, et al (2017) The ultraviolet spectrograph on NASA's Juno mission. Space Sci Rev 213:447–473. https://doi.org/10.1007/s11214-014-0040-z

Greathouse TK, Lacy JH, Bézard B, et al (2005) Meridional variations of temperature, C_2H_2 and C_2H_6 abundances in Saturn's stratosphere at southern summer solstice. Icarus 177:18–31. https://doi.org/10.1016/j.icarus.2005.02.016

Greathouse TK, Gladstone GR, Moses JI, et al (2010) New horizons Alice ultraviolet observations of a stellar occultation by Jupiter's atmosphere. Icarus 208:293–305. https://doi.org/10.1016/j.icarus.2010.02.002

Greathouse TK, Gladstone GR, Davis MW, et al (2013) Performance results from in-flight commissioning of the Juno Ultraviolet Spectrograph (Juno-UVS). In: UV, X-ray, and gamma-ray space instrumentation for astronomy XVIII, 88590T. https://doi.org/10.1117/12.2024537

Griffith CA, Bézard B, Greathouse TK, et al (1997) Thermal infrared imaging spectroscopy of Shoemaker-Levy 9 impact sites: spatial and vertical distributions of NH_3, C_2H_4, and 10-μm dust emission. Icarus 128(2):275–293. https://doi.org/10.1006/icar.1997.5752

Griffith CA, Bézard B, Greathouse T, et al (2004) Meridional transport of HCN from SL9 impacts on Jupiter. Icarus 170:58–69. https://doi.org/10.1016/j.icarus.2004.02.006

Grodent D, Waite JHJ, Gérard JC (2001) A self-consistent model of the Jovian auroral thermal structure. J Geophys Res 106(A7):12933–12952. https://doi.org/10.1029/2000JA900129

Grodent D, Clarke JT, Waite JH, et al (2003) Jupiter's polar auroral emissions. J Geophys Res Space Phys 108(A10):1366. https://doi.org/10.1029/2003JA010017

Grodent D, Bonfond B, GéRard JC, et al (2008) Auroral evidence of a localized magnetic anomaly in Jupiter's northern hemisphere. J Geophys Res Space Phys 113(A9):A09201. https://doi.org/10.1029/2008JA013185

Guerlet S, Fouchet T, Bézard B, et al (2009) Vertical and meridional distribution of ethane, acetylene and propane in Saturn's stratosphere from CIRS/Cassini limb observations. Icarus 203(1):214–232. https://doi.org/10.1016/j.icarus.2009.04.002

Guerlet S, Fouchet T, Bézard B, et al (2010) Meridional distribution of CH_3C_2H and C_4H_2 in Saturn's stratosphere from CIRS/Cassini limb and nadir observations. Icarus 209(2):682–695. https://doi.org/10.1016/j.icarus.2010.03.033

Guerlet S, Spiga A, Delattre H, et al (2020) Radiative-equilibrium model of Jupiter's atmosphere and application to estimating stratospheric circulations. Icarus 351:113935. https://doi.org/10.1016/j.icarus.2020.113935. arXiv:1907.04556 [astro-ph.EP]

Hammel HB, Beebe RF, Ingersoll AP, et al (1995) HST imaging of atmospheric phenomena created by the impact of comet Shoemaker-Levy 9. Science 267(5202):1288–1296. https://doi.org/10.1126/science.7871425

Hanel R, Conrath B, Flasar M, et al (1979a) Infrared observations of the Jovian system from Voyager 2. Science 206:952–956. https://doi.org/10.1126/science.206.4421.952

Hanel R, Conrath B, Flasar M, et al (1979b) Infrared observations of the Jovian system from Voyager 1. Science 204:972–976. https://doi.org/10.1126/science.204.4396.972

Hansen CJ, Caplinger MA, Ingersoll A, et al (2017) Junocam: Juno's outreach camera. Space Sci Rev 213(1):475–506. https://doi.org/10.1007/s11214-014-0079-x

Hill TW (1979) Inertial limit on corotation. J Geophys Res 84(A11):6554–6558. https://doi.org/10.1029/JA084iA11p06554

Hill TW (2001) The Jovian auroral oval. J Geophys Res 106(A5):8101–8108. https://doi.org/10.1029/2000JA000302

Hinson DP, Twicken JD, Karayel ET (1998) Jupiter's ionosphere: new results from Voyager 2 radio occultation measurements. J Geophys Res 103(A5):9505–9520. https://doi.org/10.1029/97JA03689

Hord CW, West RA, Simmons KE, et al (1979) Photometric observations of Jupiter at 2400 angstroms. Science 206:956–959. https://doi.org/10.1126/science.206.4421.956

Howett CJA, Irwin PGJ, Teanby NA, et al (2007) Meridional variations in stratospheric acetylene and ethane in the southern hemisphere of the saturnian atmosphere as determined from Cassini/CIRS measurements. Icarus 190(2):556–572. https://doi.org/10.1016/j.icarus.2007.03.009

Hue V, Cavalié T, Dobrijevic M, et al (2015) 2D photochemical modeling of Saturn's stratosphere. Part I: seasonal variation of atmospheric composition without meridional transport. Icarus 257:163–184. https://doi.org/10.1016/j.icarus.2015.04.001. arXiv:1504.02326 [astro-ph.EP]

Hue V, Greathouse TK, Cavalié T, et al (2016) 2D photochemical modeling of Saturn's stratosphere. Part II: feedback between composition and temperature. Icarus 267:334–343. https://doi.org/10.1016/j.icarus.2015.12.007. arXiv:1512.02724 [astro-ph.EP]

Hue V, Hersant F, Cavalié T, et al (2018) Photochemistry, mixing and transport in Jupiter's stratosphere constrained by Cassini. Icarus 307:106–123. https://doi.org/10.1016/j.icarus.2018.02.018. arXiv:1802.08697 [astro-ph.EP]

Hue V, Gladstone GR, Greathouse TK, et al (2019) In-flight characterization and calibration of the Juno-Ultraviolet Spectrograph (Juno-UVS). Astron J 157(2):90. https://doi.org/10.3847/1538-3881/aafb36

Hue V, Giles RS, Gladstone GR, et al (2021) Updated radiometric and wavelength calibration of the Juno ultraviolet spectrograph. J Astron Telesc Instrum Syst 7:044003. https://doi.org/10.1117/1.JATIS.7.4.044003

Hueso R, Sánchez-Lavega A, Fouchet T, et al (2023) An intense narrow equatorial jet in Jupiter's lower stratosphere observed by JWST. Nat Astron. https://doi.org/10.1038/s41550-023-02099-2

Johnson RE (2018) Infrared observations of Jupiter's ionosphere. PhD thesis, University of Leicester, UK

Johnson RE, Stallard TS, Melin H, et al (2017) Jupiter's polar ionospheric flows: high resolution mapping of spectral intensity and line-of-sight velocity of H_3^+ ions. J Geophys Res Space Phys 122(7):7599–7618. https://doi.org/10.1002/2017JA024176

Karkoschka E, Tomasko MG (2010) Methane absorption coefficients for the Jovian planets from laboratory, Huygens, and HST data. Icarus 205(2):674–694. https://doi.org/10.1016/j.icarus.2009.07.044

Kim YH, Fox JL (1994) The chemistry of hydrocarbon ions in the Jovian ionosphere. Icarus 112:310–325. https://doi.org/10.1006/icar.1994.1186

Kim SJ, Caldwell J, Rivolo AR, et al (1985) Infrared polar brightening on Jupiter. III - spectrometry from the Voyager 1 IRIS experiment. Icarus 64:233–248. https://doi.org/10.1016/0019-1035(85)90088-0

Kim SJ, Drossart P, Caldwell J, et al (1991) The 2-μm polar haze of Jupiter. Icarus 91(1):145–153. https://doi.org/10.1016/0019-1035(91)90133-E

Kim YH, Fox JL, Caldwell JJ (1997) Temperatures and altitudes of Jupiter's ultraviolet aurora inferred from GHRS observations with the Hubble Space Telescope. Icarus 128(1):189–201. https://doi.org/10.1006/icar.1997.5699

Kim SJ, Geballe TR, Greathouse TK, et al (2017) Temperatures and CH_4 mixing ratios near the homopause of the 8 μm North polar hot spot of Jupiter. Icarus 281:281–285. https://doi.org/10.1016/j.icarus.2016.09.017

Kliore AJ, Anderson JD, Armstrong JW, et al (2004) Cassini radio science. Space Sci Rev 115(1–4):1–70. https://doi.org/10.1007/s11214-004-1436-y

Koskinen T, Guerlet S (2018) Atmospheric structure and helium abundance on Saturn from Cassini/UVIS and cirs observations. Icarus 307:161–171. https://doi.org/10.1016/j.icarus.2018.02.020. https://www.sciencedirect.com/science/article/pii/S0019103517306553

Kostiuk T, Espenak F, Mumma MJ, et al (1989) Infrared studies of hydrocarbons on Jupiter. Infrared Phys 29:199–204. https://doi.org/10.1016/0020-0891(89)90048-1

Kostiuk T, Romani P, Espenak F, et al (1993) Temperature and abundances in the Jovian auroral stratosphere 2. Ethylene as a probe of the microbar region. J Geophys Res 98(E10):18823–18830. https://doi.org/10.1029/93JE01332

Krupp N, Lagg A, Livi S, et al (2001) Global flows of energetic ions in Jupiter's equatorial plane: first-order approximation. J Geophys Res 106(A11):26017–26032. https://doi.org/10.1029/2000JA900138

Kunde VG, Ade PA, Barney RD, et al (1996) Cassini infrared Fourier spectroscopic investigation. In: Horn L (ed) Cassini/Huygens: a mission to the Saturnian systems. Proc SPIE, vol 2803. SPIE, pp 162–177. https://doi.org/10.1117/12.253416

Kunde VG, Flasar FM, Jennings DE, et al (2004) Jupiter's atmospheric composition from the Cassini thermal infrared spectroscopy experiment. Science 305:1582–1587. https://doi.org/10.1126/science.1100240

Lacy JH, Richter MJ, Greathouse TK, et al (2002) TEXES: a sensitive high-resolution grating spectrograph for the mid-infrared. Publ Astron Soc Pac 114(792):153–168. https://doi.org/10.1086/338730. arXiv:astro-ph/0110521 [astro-ph]

Lellouch E, Paubert G, Moreno R, et al (1995) Chemical and thermal response of Jupiter's atmosphere following the impact of comet Shoemaker-Levy 9. Nature 373:592–595. https://doi.org/10.1038/373592a0

Lellouch E, Bézard B, Moreno R, et al (1997) Carbon monoxide in Jupiter after the impact of comet Shoemaker-Levy 9. Planet Space Sci 45:1203–1212. https://doi.org/10.1016/S0032-0633(97)00043-3

Lellouch E, Bézard B, Moses JI, et al (2002) The origin of water vapor and carbon dioxide in Jupiter's stratosphere. Icarus 159:112–131. https://doi.org/10.1006/icar.2002.6929

Lellouch E, Bézard B, Strobel DF, et al (2006) On the HCN and CO_2 abundance and distribution in Jupiter's stratosphere. Icarus 184:478–497. https://doi.org/10.1016/j.icarus.2006.05.018

Li C, Ingersoll A, Bolton S, et al (2020) The water abundance in Jupiter's equatorial zone. Nat Astron 4:609–616. https://doi.org/10.1038/s41550-020-1009-3. arXiv:2012.10305 [astro-ph.EP]

Liang MC, Shia RL, Lee AYT, et al (2005) Meridional transport in the stratosphere of Jupiter. Astrophys J Lett 635:L177–L180. https://doi.org/10.1086/499624. arXiv:astro-ph/0512068

Lindal GF, Wood GE, Levy GS, et al (1981) The atmosphere of Jupiter: an analysis of the Voyager radio occulation measurements. J Geophys Res 86(A10):8721–8727. https://doi.org/10.1029/JA086iA10p08721

Livengood TA, Kostiuk T, Espenak F, et al (1993) Temperature and abundances in the Jovian auroral stratosphere 1. Ethane as a probe of the millibar region. J Geophys Res 98(E10):18813–18822. https://doi.org/10.1029/93JE01043

Loison JC, Hébrard E, Dobrijevic M, et al (2015) The neutral photochemistry of nitriles, amines and imines in the atmosphere of Titan. Icarus 247:218–247. https://doi.org/10.1016/j.icarus.2014.09.039

Marten A, Gautier D, Griffin MJ, et al (1995) The collision of comet Shoemaker-Levy 9 with Jupiter: detection and evolution of HCN in the stratosphere of the planet. Geophys Res Lett 22:1589–1592. https://doi.org/10.1029/95GL00949

Melin H, Miller S, Stallard T, et al (2005) Non-LTE effects on H_3^+ emission in the Jovian upper atmosphere. Icarus 178(1):97–103. https://doi.org/10.1016/j.icarus.2005.04.016

Melin H, Fletcher LN, Donnelly PT, et al (2018) Assessing the long-term variability of acetylene and ethane in the stratosphere of Jupiter. Icarus 305:301–313. https://doi.org/10.1016/j.icarus.2017.12.041. arXiv:1801.00652 [astro-ph.EP]

Melin H, Fletcher LN, Irwin PGJ, et al (2020) Jupiter in the ultraviolet: acetylene and ethane abundances in the stratosphere of Jupiter from Cassini observations between 0.15 and 0.19 μm. Astron J 159(6):291. https://doi.org/10.3847/1538-3881/ab91a6. arXiv:2005.09895 [astro-ph.EP]

Moreno F, Sedano J (1997) Radiative balance and dynamics in the stratosphere of Jupiter: results from a latitude-dependent aerosol heating model. Icarus 130:36–48. https://doi.org/10.1006/icar.1997.5787

Moreno R, Marten A, Matthews HE, et al (2003) Long-term evolution of CO, CS and HCN in Jupiter after the impacts of comet Shoemaker-Levy 9. Planet Space Sci 51:591–611. https://doi.org/10.1016/S0032-0633(03)00072-2

Moses JI (1996) SL9 impact chemistry: long-term photochemical evolution. In: Noll KS, Weaver HA, Feldman PD (eds) The collision of comet Shoemaker-Levy 9 and Jupiter. IAU Colloquium, vol 156. Cambridge University Press, pp 243–268. https://doi.org/10.1017/CBO9780511525056.013

Moses JI, Greathouse TK (2005) Latitudinal and seasonal models of stratospheric photochemistry on Saturn: comparison with infrared data from IRTF/TEXES. J Geophys Res, Planets 110(E9):E09007. https://doi.org/10.1029/2005JE002450

Moses JI, Poppe AR (2017) Dust ablation on the giant planets: consequences for stratospheric photochemistry. Icarus 297:33–58. https://doi.org/10.1016/j.icarus.2017.06.002. arXiv:1706.04686 [astro-ph.EP]

Moses JI, Allen M, Gladstone GR (1995) Nitrogen and oxygen photochemistry following SL9. Geophys Res Lett 22(12):1601–1604. https://doi.org/10.1029/95GL01199

Moses JI, Bézard B, Lellouch E, et al (2000) Photochemistry of Saturn's atmosphere. I. Hydrocarbon chemistry and comparisons with ISO observations. Icarus 143(2):244–298. https://doi.org/10.1006/icar.1999.6270

Moses JI, Fouchet T, Bézard B, et al (2005a) Photochemistry and diffusion in Jupiter's stratosphere: constraints from ISO observations and comparisons with other giant planets. J Geophys Res, Planets 110:E08001. https://doi.org/10.1029/2005JE002411

Moses JI, Fouchet T, Bézard B, et al (2005b) Photochemistry and diffusion in Jupiter's stratosphere: constraints from ISO observations and comparisons with other giant planets. J Geophys Res, Planets 110(E8):E08001. https://doi.org/10.1029/2005JE002411

Nixon CA, Achterberg RK, Conrath BJ, et al (2007) Meridional variations of C_2H_2 and C_2H_6 in Jupiter's atmosphere from Cassini CIRS infrared spectra. Icarus 188:47–71. https://doi.org/10.1016/j.icarus.2006.11.016

Nixon CA, Achterberg RK, Romani PN, et al (2010) Abundances of Jupiter's trace hydrocarbons from Voyager and Cassini. Planet Space Sci 58:1667–1680. https://doi.org/10.1016/j.pss.2010.05.008. arXiv:1005.3959 [astro-ph.EP]

O'Donoghue J, Moore L, Bhakyapaibul T, et al (2021) Global upper-atmospheric heating on Jupiter by the polar aurorae. Nature 596(7870):54–57. https://doi.org/10.1038/s41586-021-03706-w

Orton GS, Friedson AJ, Caldwell J, et al (1991) Thermal maps of Jupiter - spatial organization and time dependence of stratospheric temperatures, 1980 to 1990. Science 252:537–542. https://doi.org/10.1126/science.252.5005.537

Parkinson CD, Stewart AIF, Wong AS, et al (2006) Enhanced transport in the polar mesosphere of Jupiter: evidence from Cassini UVIS helium 584 Å airglow. J Geophys Res, Planets 111(E2):E02002. https://doi.org/10.1029/2005JE002539

Perrin Z, Carrasco N, Chatain A, et al (2021) An atmospheric origin for hcn-derived polymers on Titan. Processes 9(6):965. https://www.mdpi.com/2227-9717/9/6/965. https://doi.org/10.3390/pr9060965

Perry JJ, Kim YH, Fox JL, et al (1999) Chemistry of the Jovian auroral ionosphere. J Geophys Res 104:16541–16566. https://doi.org/10.1029/1999JE900022

Porco CC, West RA, McEwen A, et al (2003) Cassini imaging of Jupiter's atmosphere, satellites, and rings. Science 299(5612):1541–1547. https://doi.org/10.1126/science.1079462

Porco CC, West RA, Squyres S, et al (2004) Cassini imaging science: instrument characteristics and anticipated scientific investigations at Saturn. Space Sci Rev 115(1–4):363–497. https://doi.org/10.1007/s11214-004-1456-7

Prather MJ, Logan JA, McElroy MB (1978) Carbon monoxide in Jupiter's upper atmosphere: an extraplanetary source. Astrophys J 223:1072–1081. https://doi.org/10.1086/156340

Prinn RG, Barshay SS (1977) Carbon monoxide on Jupiter and implications for atmospheric convection. Science 198(4321):1031–1034. https://doi.org/10.1126/science.198.4321.1031

Pryor WR, Hord CW (1991) A study of photopolarimeter system UV absorption data on Jupiter, Saturn, Uranus, and Neptune: implications for auroral haze formation. Icarus 91(1):161–172. https://doi.org/10.1016/0019-1035(91)90135-G

Rages K, Beebe R, Senske D (1999) Jovian stratospheric hazes: the high phase angle view from Galileo. Icarus 139(2):211–226. https://doi.org/10.1006/icar.1999.6103

Ray LC, Achilleos NA, Yates JN (2015) The effect of including field-aligned potentials in the coupling between Jupiter's thermosphere, ionosphere, and magnetosphere. J Geophys Res Space Phys 120(8):6987–7005. https://doi.org/10.1002/2015JA021319

Rego D, Achilleos N, Stallard T, et al (1999) Supersonic winds in Jupiter's aurorae. Nature 399(6732):121–124. https://doi.org/10.1038/20121

Ridgway ST (1974) Jupiter: identification of ethane and acetylene. Astrophys J Lett 187:L41–L43. https://doi.org/10.1086/181388

Ridgway ST, Brault JW (1984) Astronomical Fourier transform spectroscopy revisited. Annu Rev Astron Astrophys 22:291–317. https://doi.org/10.1146/annurev.aa.22.090184.001451

Robinson TD, Catling DC (2014) Common 0.1 bar tropopause in thick atmospheres set by pressure-dependent infrared transparency. Nat Geosci 7(1):12–15. https://doi.org/10.1038/ngeo2020. arXiv:1312.6859 [astro-ph.EP]

Rodriguez-Ovalle P, Fouchet T, De Pater I, et al (2023) Mid infrared analysis of Jupiter South Pole from JWST MIRI-MRS observations: thermo-chemical disturbances caused by auroral activity. In: EGU General Assembly Conference Abstracts, EGU–12,471. https://doi.org/10.5194/egusphere-egu23-12471

Rodríguez-Ovalle P, Fouchet T, Guerlet S, et al (2024) Temperature and composition disturbances in the southern auroral region of Jupiter revealed by JWST/MIRI. J Geophys Res, Planets 129(6):e2024JE008299. https://doi.org/10.1029/2024JE008299. arXiv:2406.08133 [astro-ph.EP]

Rogers JH, Eichstädt G, Hansen CJ, et al (2022) Flow patterns of Jupiter's south polar region. Icarus 372:114742. https://doi.org/10.1016/j.icarus.2021.114742

Roman MT (2023) Mid-infrared observations of the giant planets. Remote Sens 15(7):1811. https://doi.org/10.3390/rs15071811. arXiv:2303.16264 [astro-ph.EP]

Sada PV, Bjoraker GL, Jennings DE, et al (1998) Observations of CH_4, C_2H_6, and C_2H_2 in the stratosphere of Jupiter. Icarus 136:192–201. https://doi.org/10.1006/icar.1998.6021

Sanchez-Lavega A, Hueso R, Ramón Acarreta J (1998) A system of circumpolar waves in Jupiter's stratosphere. Geophys Res Lett 25(21):4043–4046. https://doi.org/10.1029/1998GL900059

Sánchez-Lavega A, Orton GS, Hueso R, et al (2008) Depth of a strong Jovian jet from a planetary-scale disturbance driven by storms. Nature 451(7177):437–440. https://doi.org/10.1038/nature06533

Sánchez-Lavega A, Legarreta J, García-Melendo E, et al (2013) Colors of Jupiter's large anticyclones and the interaction of a tropical red oval with the great red spot in 2008. J Geophys Res, Planets 118(12):2537–2557. https://doi.org/10.1002/2013JE004371

Sinclair JA, Irwin PGJ, Fletcher LN, et al (2013) Seasonal variations of temperature, acetylene and ethane in Saturn's atmosphere from 2005 to 2010, as observed by Cassini-CIRS. Icarus 225(1):257–271. https://doi.org/10.1016/j.icarus.2013.03.011

Sinclair JA, Orton GS, Greathouse TK, et al (2017) Jupiter's auroral-related stratospheric heating and chemistry I: analysis of Voyager-IRIS and Cassini-CIRS spectra. Icarus 292:182–207. https://doi.org/10.1016/j.icarus.2016.12.033

Sinclair JA, Orton GS, Greathouse TK, et al (2018) Jupiter's auroral-related stratospheric heating and chemistry II: analysis of IRTF-TEXES spectra measured in December 2014. Icarus 300:305–326. https://doi.org/10.1016/j.icarus.2017.09.016

Sinclair JA, Moses JI, Hue V, et al (2019) Jupiter's auroral-related stratospheric heating and chemistry III: abundances of C_2H_4, CH_3C_2H, C_4H_2 and C_6H_6 from Voyager-IRIS and Cassini-CIRS. Icarus 328:176–193. https://doi.org/10.1016/j.icarus.2019.03.012

Sinclair JA, Greathouse TK, Giles RS, et al (2020) Spatial variations in the altitude of the CH_4 homopause at Jupiter's mid-to-high latitudes, as constrained from IRTF-TEXES spectra. Planet Sci J 1(3):85. https://doi.org/10.3847/PSJ/abc887

Sinclair JA, Greathouse TK, Giles RS, et al (2023) A high spatial and spectral resolution study of Jupiter's mid-infrared auroral emissions and their response to a solar wind compression. Planet Sci J 4(4):76. https://doi.org/10.3847/PSJ/accb95. arXiv:2304.08390 [astro-ph.EP]

Smith CGA, Aylward AD (2009) Coupled rotational dynamics of Jupiter's thermosphere and magnetosphere. Ann Geophys 27(1):199–230. https://doi.org/10.5194/angeo-27-199-2009

Stallard T, Miller S, Millward G, et al (2001) On the dynamics of the Jovian ionosphere and thermosphere. I. The measurement of ion winds. Icarus 154(2):475–491. https://doi.org/10.1006/icar.2001.6681

Stallard TS, Miller S, Cowley SWH, et al (2003) Jupiter's polar ionospheric flows: measured intensity and velocity variations poleward of the main auroral oval. Geophys Res Lett 30(5):1221. https://doi.org/10.1029/2002GL016031

Strobel DF (1969) The photochemistry of methane in the Jovian atmosphere. J Atmos Sci 26:906–911. https://doi.org/10.1175/1520-0469(1969)026<0906:TPOMIT>2.0.CO;2

Strobel DF (1973) The photochemistry of hydrocarbons in the Jovian atmosphere. J Atmos Sci 30:489–498. https://doi.org/10.1175/1520-0469(1973)030<0489:TPOHIT>2.0.CO;2

Strobel DF, Yung YL (1979) The Galilean satellites as a source of CO in the Jovian upper atmosphere. Icarus 37(1):256–263. https://doi.org/10.1016/0019-1035(79)90130-1

Sundstrom G, Mowat JR, Danared H, et al (1994) Destruction rate of H_3ˆ+ by low-energy electrons measured in a storage-ring experiment. Science 263(5148):785–787. https://doi.org/10.1126/science.263.5148.785

Sylvestre M, Guerlet S, Fouchet T, et al (2015) Seasonal changes in Saturn's stratosphere inferred from Cassini/CIRS limb observations. Icarus 258:224–238. https://doi.org/10.1016/j.icarus.2015.05.025

Tao C, Fujiwara H, Kasaba Y (2009) Neutral wind control of the Jovian magnetosphere-ionosphere current system. J Geophys Res Space Phys 114(A8):A08307. https://doi.org/10.1029/2008JA013966

Tao C, Badman SV, Fujimoto M (2011) UV and IR auroral emission model for the outer planets: Jupiter and Saturn comparison. Icarus 213:581–592. https://doi.org/10.1016/j.icarus.2011.04.001

Thomas N, Bagenal F, Hill TW, et al (2004) The Io neutral clouds and plasma torus. In: Bagenal F, Dowling TE, McKinnon WB (eds) Jupiter: The planet, satellites and magnetosphere. Cambridge University Press, pp 561–591

Tokunaga AT, Beck SC, Geballe TR, et al (1981) The detection of HCN on Jupiter. Icarus 48(2):283–289. https://doi.org/10.1016/0019-1035(81)90109-3

Tomasko MG, Karkoschka E, Martinek S (1986) Observations of the limb darkening of Jupiter at ultraviolet wavelengths and constraints on the properties and distribution of stratospheric aerosols. Icarus 65(2–3):218–243. https://doi.org/10.1016/0019-1035(86)90136-3

Toon OB, Turco RP, Westphal D, et al (1988) A multidimensional model for aerosols - description of computational analogs. J Atmos Sci 45:2123–2143. https://doi.org/10.1175/1520-0469(1988)045<2123:AMMFAD>2.0.CO;2

Tsubota T, Wong M, Stallard T, et al (2024) UV-Dark Polar Ovals on Jupiter Trace the Depth of Magnetosphere-Atmosphere Connection. Nature Astronomy

Vincent MB, Clarke JT, Ballester GE, et al (2000) Jupiter's polar regions in the ultraviolet as imaged by HST/WFPC2: auroral-aligned features and zonal motions. Icarus 143(2):205–222. https://doi.org/10.1006/icar.1999.6233

Visscher C, Moses JI, Saslow SA (2010) The deep water abundance on Jupiter: new constraints from thermochemical kinetics and diffusion modeling. Icarus 209(2):602–615. https://doi.org/10.1016/j.icarus.2010.03.029. arXiv:1003.6077 [astro-ph.EP]

Wang H, Frenklach M (1994) Calculations of rate coefficients for the chemically activated reactions of acetylene with vinylic and aromatic radicals. J Phys Chem 98(44):11465–11489. https://doi.org/10.1021/j100095a033

Wang R, Stallard TS, Melin H, et al (2023) Asymmetric ionospheric jets in Jupiter's aurora. J Geophys Res Space Phys 128(12):e2023JA031861. https://doi.org/10.1029/2023JA031861

West RA, Strobel DF, Tomasko MG (1986) Clouds, aerosols, and photochemistry in the Jovian atmosphere. Icarus 65(2–3):161–217. https://doi.org/10.1016/0019-1035(86)90135-1

West RA, Friedson AJ, Appleby JF (1992) Jovian large-scale stratospheric circulation. Icarus 100:245–259. https://doi.org/10.1016/0019-1035(92)90033-4

West RA, Baines KH, Friedson AJ, et al (2004) Jovian clouds and haze. In: Bagenal F, Dowling TE, McKinnon WB (eds) Jupiter: The planet, satellites and magnetosphere. Cambridge University Press, pp 79–104

Wong AS, Lee AYT, Yung YL, et al (2000) Jupiter: aerosol chemistry in the polar atmosphere. Astrophys J Lett 534:L215–L217. https://doi.org/10.1086/312675

Wong AS, Yung YL, Friedson AJ (2003) Benzene and haze formation in the polar atmosphere of Jupiter. Geophys Res Lett 30:1447. https://doi.org/10.1029/2002GL016661

Wong MH, Simon AA, Tollefson JW, et al (2020) High-resolution UV/optical/IR imaging of Jupiter in 2016-2019. Astrophys J Suppl Ser 247(2):58. https://doi.org/10.3847/1538-4365/ab775f

Yates JN, Achilleos N, Guio P (2012) Influence of upstream solar wind on thermospheric flows at Jupiter. Planet Space Sci 61(1):15–31. https://doi.org/10.1016/j.pss.2011.08.007. arXiv:1012.3411 [astro-ph.EP]

Yelle RV, Young LA, Vervack RJ, et al (1996) Structure of Jupiter's upper atmosphere: predictions for Galileo. J Geophys Res 101:2149–2162. https://doi.org/10.1029/95JE03384

Yung YL, Allen M, Pinto JP (1984) Photochemistry of the atmosphere of Titan - comparison between model and observations. Astrophys J 55:465–506. https://doi.org/10.1086/190963

Yung YL, Drew WA, Pinto JP, et al (1988) Estimation of the reaction rate for the formation of CH_3O from $H + H_2CO$: implications for chemistry in the Solar System. Icarus 73(3):516–526. https://doi.org/10.1016/0019-1035(88)90061-9

Zahnle K (1996) Dynamics and chemistry of SL9 plumes. In: Noll KS, Weaver HA, Feldman PD (eds) The collision of comet Shoemaker-Levy 9 and Jupiter. IAU Colloquium, vol 156. Cambridge University Press, pp 183–212. https://doi.org/10.1017/CBO9780511525056.011

Zhang X, West RA, Banfield D, et al (2013) Stratospheric aerosols on Jupiter from Cassini observations. Icarus 226:159–171. https://doi.org/10.1016/j.icarus.2013.05.020

Zube NG, Zhang X, Li T, et al (2021) Radiative-dynamical simulation of Jupiter's stratosphere and upper troposphere. Astrophys J 921(2):174. https://doi.org/10.3847/1538-4357/ac1e95

Authors and Affiliations

V. Hue[1] · T. Cavalié[2,3] · J.A. Sinclair[4] · X. Zhang[5] · B. Benmahi[6] · P. Rodríguez-Ovalle[3] · R.S. Giles[7] · T.S. Stallard[8] · R.E. Johnson[9] · M. Dobrijevic[2] · T. Fouchet[3] · T.K. Greathouse[7] · D.C. Grodent[6] · R. Hueso[10] · O. Mousis[1] · C.A. Nixon[11]

✉ V. Hue
vincent.hue@lam.fr

1 Aix-Marseille Université, CNES, Institut Origines, LAM, Marseille, France

2 Laboratoire d'Astrophysique de Bordeaux, Univ. Bordeaux, CNRS, B18N, allée Geoffroy Saint-Hilaire, 33615 Pessac, France

3 LESIA, Observatoire de Paris, Université PSL, Sorbonne Université, Université Paris Cité, CNRS, 5 place Jules Janssen, 92195 Meudon, France

4 Jet Propulsion Laboratory, California Institute of Technology, 4800 Oak Grove Dr, Pasadena, CA 91109, USA

5 Department of Earth and Planetary Sciences, University of California Santa Cruz, Santa Cruz, CA 95064, USA

6 Laboratory for Planetary and Atmospheric Physics, STAR Institute, University of Liege, Liege, Belgium

7 Space Science and Engineering Division, Southwest Research Institute, San Antonio, TX, USA

8 Department of Mathematics, Physics and Electrical Engineering, Northumbria University, Newcastle upon Tyne, UK

9 Department of Physics, Aberystwyth University, Ceredigion, UK

10 Escuela de Ingeniería de Bilbao, Universidad del País Vasco, UPV/EHU, Bilbao, Spain

11 Solar System Exploration Division, NASA Goddard Space Flight Center, Greenbelt, MD 20771, USA